Biogeosciences Discuss., 6, 7231–7293, 2009
www.biogeosciences-discuss.net/6/7231/2009/

Biogeosciences Discussions

Biogeosciences Discussions is the access reviewed discussion forum of *Biogeosciences*

A model-based assessment of the TrOCA approach for estimating oceanic anthropogenic carbon

A. Yool[1], **A. Oschlies**[2], **and A. J. G. Nurser**[1]

[1]National Oceanography Centre, Southampton; University of Southampton Waterfront Campus, European Way, Southampton SO14 3ZH, UK
[2]IFM-GEOMAR, Leibniz Institute of Marine Sciences; Düsternbrooker Weg 20, 24105 Kiel, Germany

Received: 11 June 2009 – Accepted: 23 June 2009 – Published: 21 July 2009

Correspondence to: A. Yool (axy@noc.soton.ac.uk)

Published by Copernicus Publications on behalf of the European Geosciences Union.

Abstract

The future behaviour of the global ocean as a sink for CO_2 is significant for climate change, but it is also important to understand its past by quantifying anthropogenic CO_2 (C_{ant}) in the ocean today. Unfortunately, this is complicated by the difficulty of deconvoluting C_{ant} from the natural, unperturbed carbon cycle. Nonetheless, a range of techniques have been devised that perform this separation using the information implicit in other physical, biogeochemical and artificial ocean tracers. One such method is the TrOCA approach, whose parameterisation is derived from relationships between biogeochemical tracers within watermasses defined by age tracers such as CFC-11. TrOCA has a number of methodological advantages, and has been shown to be plausible, relative to other methods, in a number of studies. Here we examine the TrOCA approach by using it to deconvolute the known distribution of C_{ant} from an ocean general circulation model (OGCM) simulation of the industrial period (1864–2004). TrOCA is evaluated at local, regional and global scales, with an emphasis on the wider applicability of the parameterisations derived at these scales. Our work finds that the published TrOCA parameterisation performs poorly when extrapolated beyond its calibration region, either with observational data or (especially) model output. Optimising TrOCA parameters using model output as a synthetic dataset leads to some small improvements, but the resulting TrOCA variants still perform poorly. Furthermore, there are large ranges on the optimised TrOCA parameters suggesting that a "universal" TrOCA parameterisation is not achieveable.

1 Introduction

Since the beginning of the Industrial Revolution, atmospheric CO_2 concentrations have been rising in response to human activities such as fossil fuel combustion, deforestation, land-use changes and cement production. However, the rise in atmospheric CO_2 has not paralleled anthropogenic emissions, since a significant fraction of the CO_2

BGD

6, 7231–7293, 2009

released to the atmosphere has been removed to reservoirs on the land and, particularly, in the ocean (Revelle and Seuss, 1957). In terms of the Earth's climate, since C_{ant} that is transferred to land or ocean sinks cannot cause global warming (though it does cause ocean acidification; e.g. Orr et al., 2005) there is continuing interest in establishing the capacity and uptake rate of these reservoirs. In the long-term (a thousand years or more) the majority of C_{ant} will be absorbed by the ocean through dissolution enhanced by processes including shoaling of the calcium carbonate compensation depth and silicate weathering (Archer, 2005), but there is still considerable uncertainty in the role that these reservoirs will play in the near future (Friedlingstein et al., 2006).

A key aspect of understanding the future behaviour of the ocean as a sink for CO_2 is determining this role in the recent past. Fossil fuel CO_2 has been accumulating in the atmosphere for more than two hundred years, with the majority of this increase occurring during the twentieth century. Consequently, the ocean has been absorbing this C_{ant} over the corresponding period. However, quantifying the ocean's role is complicated by the difficulty of separating C_{ant} from that of the natural carbon cycle (which, given relatively stable atmospheric pCO_2 prior to the Industrial Revolution, is assumed to be in quasi-equilibrium). While there are signals in the distributions of the carbon isotopes ^{13}C (Sonnerup et al., 2007) and ^{14}C (Fallon et al., 2003), most methodologies for distinguishing C_{ant} utilise physical, biogeochemical and/or artificial tracers to guide them.

The first methods devised were based on back-calculation methods (Brewer, 1978; Chen and Millero, 1979) that used oxygen, nutrient and dissolved inorganic carbon (DIC) concentrations, together with a series of biogeochemical assumptions, to separate the C_{ant} signal from the background DIC. The assumptions used relate to biogeochemical processes including calcium carbonate precipitation and dissolution, and the production and remineralisation of organic material. These methods, with some varying details, have been used in a number of studies for different locations, and for a range of different applications, including Chen and Pythkiwicz (1979), Papaud and

BGD
6, 7231–7293, 2009

Poisson (1986), Goyet and Brewer (1993), Tsunogai et al. (1993), Perez et al. (2002) and Lo Monaco et al. (2005).

Since the biogeochemical back-calculation approach involves a number of uncertainties, it was improved upon by the development of the ΔC^* method (Gruber et al., 1996) that additionally accounted for the disequilibrium between dissolved CO_2 and the atmosphere at the point when a water parcel became isolated from the air-sea interface. The ΔC^* approach, initially developed using North Atlantic observations, has been modified for the Indian (Sabine et al., 1999) and Pacific (Sabine et al., 2002) basins and for the global ocean (Key et al., 2004). Subsequent work has both introduced improvements to the method (e.g., Gruber, 1998) and evaluated uncertainties with ΔC^* (Matsumoto and Gruber, 2005).

Tracer combining **O**xygen, inorganic **C**arbon and total **A**lkalinity (TrOCA) was initially developed as a conservative tracer to aid the distinguishing of watermasses, that was complementary to other composite tracers such as ΔC^* (Touratier and Goyet, 2004a). The TrOCA method has subsequently been used to quantify C_{ant} in the Atlantic (Touratier and Goyet, 2004b; Touratier et al., 2005) Indian (Touratier et al., 2007; Alvarez et al., 2009) and Southern (Lo Monaco et al., 2005; Sandrini et al., 2007) oceans, and to infer regional air-sea CO_2 fluxes (Gerber et al., 2009). Aspects of the parameterisation of the TrOCA model mean that it is less sensitive to some factors that are known to cause uncertainty in other methods for estimating C_{ant}, including variable air-sea CO_2 disequilibrium and significant diapycnal mixing (Touratier and Goyet, 2004a).

Since it is not possible to directly discern C_{ant} from natural DIC in observational data, the deconvolution methods above only produce estimates of the distribution of C_{ant}. By attempting to simulate the ocean's carbon cycle, OGCMs both provide an alternative approach to estimating oceanic uptake of CO_2, and a synthetic dataset against which deconvolution methods can be examined (Matsumoto and Gruber, 2005). In this work, the TrOCA method is examined using synthetic data generated via this latter mode. The analysis focuses on the regional and global applicability of TrOCA, and on certain

of its key assumptions.

The paper is organised as follows. The *Methods* section first introduces the model used to provide synthetic dataset, including its physical and biogeochemical representation of the ocean, and details of the simulation. Next, the *Methods* section describes the TrOCA method itself, with a focus on its key parameters and its calibration from observational data. The *Results and Discussion* section describes the application of the TrOCA method first to the locale in which it was calibrated, and then to global scale observations and the modelled synthetic dataset. This section then examines the re-optimisation of the TrOCA method using synthetic data, and several sensitivity analyses to assess its performance. Finally, the paper concludes with a summary of our findings.

2 Methods

2.1 Ocean general circulation model

2.1.1 Physical model

The work described here makes use of OCCAM, a global, medium-resolution, primitive equation, finite difference ocean general circulation model (a high-resolution version is described in Marsh et al., 2005). OCCAM's vertical resolution is 66 levels (with thickness ranging from 5 m at the surface to 200 m at the abyssal seafloor), with a horizontal resolution of typically 1°. A distinctive feature of OCCAM is its organisation onto two horizontal grids to avoid grid-spacing difficulties close to the North Pole singularity. Grid 1 encompasses the Pacific, Indian, Southern and South Atlantic oceans, while grid 2 covers the North Atlantic and Arctic sea. This arrangement brings the two grids into alignment along the equator in the Atlantic basin. A simple channel model connects the two grids at the Bering Straits. OCCAM's prognostic variables are potential temperature, salinity, velocity and free-surface height.

BGD
6, 7231–7293, 2009

OCCAM includes an elastic-viscous-plastic sea-ice scheme, a K-profile parameterisation (KPP) mixed layer and Gent-McWilliams eddy parameterisation. Advection is 4th order accurate (a modified split-quick scheme), and the model employs fractional bottom gridboxes to allow a more realistic representation of bathymetry. OCCAM is time-integrated using a forward leapfrog scheme with a timestep of 1 h. Surface fluxes of heat, freshwater and momentum are not specified directly, but are calculated using empirical formulae and NCEP-derived basic atmospheric boundary layer quantities (Large and Yeager, 2004). Local daylength is calculated and used in conjunction with daily-averaged irradiance to reconstruct a realistic diel cycle. To compensate for deficiencies in the freshwater flux balance, surface salinity is relaxed towards monthly observations.

Simulations are forced at the surface with high resolution spatial and temporal data for the period January 1958 to December 2004 inclusive. Spin-up cycles made repeated use of this period (i.e. upon reaching 2004, the model state was "recycled" to 1958). Although this approach tends to warm the ocean, in practice this trend is small (Yool and Sinha, 2006).

2.1.2 Biogeochemical model

Biogeochemical cycles of nitrogen, carbon, oxygen and alkalinity are embedded within OCCAM. These cycles are driven primarily by a nitrogen-based nutrient-phytoplankton-zooplankton-detritus (NPZD) model (Oschlies, 2001) that has been coupled to the other elemental cycles (Sinha and Yool, 2006; Yool and Sinha, 2006; following Anderson and Pondaven, 2003). The adaptations necessary for this coupling include: C:N:O_2 Redfield relationships for phytoplankton and zooplankton (Anderson, 1995; Palmer and Totterdell, 2001); a separate state variable for detrital carbon (Anderson and Pondaven, 2003); a simplified scheme for biogenic calcium carbonate production and dissolution (Najjar and Orr, 1999; Najjar et al., 2007); and subroutines to calculate the air-sea exchange of CO_2 and oxygen (Orr et al., 1999b; Najjar and Orr, 1999). The model also incorporates a variable detrital sinking velocity (Schmittner et al., 2005).

The resulting model is comprised of eight tracer variables that are entirely passive and distributed throughout the model domain. A unified set of equations governs the biogeochemical tendencies throughout the water column, and these are described in the Appendix. Minor variants of this ecosystem model have previously been used within the OCCAM GCM in a number of unrelated studies, including Yool et al. (2007), Glessmer et al. (2008) and Yool et al. (2009).

In addition to the main biogeochemical tracers, OCCAM includes a series of natural, artificial and idealised tracers, including the radioisotope ^{14}C, haloalkanes and numerical ventilation tracers. ^{14}C is modelled using the protocols defined by the OCMIP-2 project (Orr et al., 1999b), and is forced by the time-history of atmospheric ^{14}C (including both the Suess Effect and twentieth century nuclear tests). Modelled haloalkanes include CFC-11, CFC-12, CFC-113 and carbon tetrachloride (CCl_4), and these are forced by atmospheric time-histories from 1910 (when CCl_4 first appears in the atmosphere; Walker et al., 2000). Air-sea exchange of haloalkanes uses the protocols defined by the OCMIP-2 project (Warner and Weiss, 1985; Zheng et al., 1998; Orr et al., 1999a). The idealised ventilation tracer ages a one day per day throughout the model domain, but is destroyed at the ocean's surface.

2.1.3 Simulation

The OCCAM configuration described above was initialised from rest with tracer fields from the World Ocean Atlas 2001 (potential temperature, salinity, nitrate, oxygen; Conkright et al., 2002) and GLODAP (carbon, alkalinity, ^{14}C; Key et al., 2004) climatologies. Biological tracers (phytoplankton, zooplankton, detritus) were initialised to arbitrary small values. CFC and ventilation tracer fields were initialised to zero.

After an initial spin-up cycle (using surface forcing data from 1958–2004; see above), the simulation underwent three further forcing cycles during which the time-history of atmospheric CO_2 (and $\Delta^{14}C$) from 1864 to 2004 was applied. A parallel "pre-industrial" DIC tracer was run alongside that exposed to the anthropogenic CO_2 transient as a control to permit the separation of natural and anthropogenic carbon. This control

experienced a constant atmospheric pCO_2 of 288.4 ppm, that of the atmosphere at 1864. This concentration is slightly higher than the generally assumed pre-industrial value (278 ppm), but has the advantage of removing approximately 100 years of gradually rising pCO_2. It was assumed that the climatic effects of CO_2 on model forcing fields are relatively small during the period 1958–2004, so that this high quality forcing data can be used for periods pre-1958. Atmospheric concentrations of haloalkanes increased according to their relevant time-histories from 1910.

2.2 TrOCA method

2.2.1 Overview

This section provides an overview of the TrOCA method. The method described is based upon the most recent version of the TrOCA method (Touratier et al., 2007), but see also the original formulation (Touratier and Goyet, 2004a) for a more comprehensive description.

The TrOCA tracer is derived from the Redfield relationships that occur between carbon, oxygen and key nutrients. Equation (1) shows an example of this stoichiometry for the processes of organic production (left to right) and remineralisation (right to left):

$$106\ CO_2 + 16\ NO_3^- + HPO_4^{2-} + 122\ H_2O + 18\ H^+ \rightleftharpoons (C_{106}H_{263}O_{110}N_{16}P) + 138\ O_2 \quad (1)$$

This equation can be rewritten to express the relationships between its coefficients:

$$\psi_C CO_2 + \psi_N NO_3^- + \psi_P HPO_4^{2-} + \psi_{H_2O} H_2O + \psi_H H^+ \rightleftharpoons \left[C_{(\psi_C)}H_{(\psi_P+2\psi_{H_2O}+\psi_H)}O_{(2\psi_C+3\psi_N+4\psi_P+\psi_{H_2O}-2\psi_{O_2})}N_{(\psi_N)}P_{(\psi_P)}\right] + \psi_{O_2} O_2 \quad (2)$$

At depth, variations in the concentration of DIC are ascribed to respiration of organic material (the backward reaction above) and the dissolution of carbonate biominerals. Applying Eq. (2), and accounting for this dissolution of calcium carbonate (estimated

from changes to alkalinity, A_T; Brewer, 1978), the concentration of DIC at depth, C_T, is approximated as:

$$C_T = \frac{\psi_C}{\psi_{O_2}} O_2 + \frac{1}{2}\left[A_T + \frac{(\psi_H - \psi_P)}{\psi_{O_2}} O_2\right] \quad (3)$$

The above relationship between biotically induced changes in C_T, O_2 and A_T can be used to define an approximately conservative "**Tr**acer combining **O**xygen, inorganic **C**arbon and total **A**lkalinity" (TrOCA):

$$\mathrm{TrOCA} = O_2 + a\left(C_T - \frac{A_T}{2}\right), \quad (4)$$

where:

$$a = \frac{\psi_{O_2}}{\psi_C + \frac{1}{2}(\psi_H - \psi_P)} \quad (5)$$

In the absence of C_{ant}, the natural (=background) value of TrOCA, TrOCA^0, is defined as a function of the natural (=background) concentrations of carbon, C_T^0, oxygen, O_2^0, and alkalinity, A_T^0:

$$\mathrm{TrOCA}^0 = O_2^0 + a\left(C_T^0 - \frac{A_T^0}{2}\right) \quad (6)$$

Using TrOCA and TrOCA^0, and assuming that neither oxygen nor alkalinity fields are substantially perturbed by anthropogenic effects (which is not exactly correct in the case of oxygen; Manning and Keeling, 2006), C_{ant} can then be estimated:

$$C_{ant}^{\mathrm{TrOCA}} = \frac{\mathrm{TrOCA} - \mathrm{TrOCA}^0}{a} \quad (7)$$

BGD
6, 7231–7293, 2009

In the original definition of the TrOCA method, $TrOCA^0$ was fitted as a function of potential temperature, θ (Touratier and Goyet, 2004a), but this was extended by Touratier et al. (2007) to include A_T. The fitting procedure requires datasets in which C_{ant} is known, and this is achieved here utilising watermass age information present in $\Delta^{14}C$ and CFC-11.

Firstly, $\Delta^{14}C$ is used to identify watermasses that are unambiguously free of C_{ant}. Waters with a value less than −175‰ are much older (>1000 years) than the industrial era (≃250 years), so should contain no C_{ant} (i.e. it is assumed that C_{ant} =0). The values of C_T, A_T and O_2 in these watermasses are used with Eqs. (4) and (5) to calculate $TrOCA^0$.

Next, estimated atmospheric CFC-11 partial pressure (pptv) is back-calculated from ambient oceanic concentrations of CFC-11 (assuming oceanic saturation; Warner and Weiss, 1985), and used to identify waters in contact with the atmosphere at the time of peak atmospheric CFC-11 concentration (1992–1995; approximately 263–271 pptv). The values of θ, S and A_T in these watermasses are then used to calculate saturation C_T concentrations for the corresponding atmospheric pCO_2 , C_T^{p357} (1992–1995; approximately 357 ppmv), and for pre-industrial conditions, C_T^{p280} (approximately 280 ppmv). Although C_T may not be at saturation concentration, this calculation instead assumes that local disequilibrium is the same under pre-industrial and anthropogenic transient conditions. The saturation concentrations are then used to estimate local C_{ant} for the period 1992–1995:

$$C_{ant92/95}^{TrOCA} = C_T^{p357} - C_T^{p280} \quad (8)$$

$TrOCA^0$is then be calculated for these watermasses using TrOCA Eq. (4). The resulting $TrOCA^0$dataset is then fitted as an exponential function of θ and A_T:

$$TrOCA^0 = f \exp\left(b + c\theta + \frac{d}{A_T^2}\right) \quad (9)$$

BGD
6, 7231–7293, 2009

The choice of this functional relationship with θ is based on its strong correlation with the TrOCA tracer, a relationship that was found to be fitted best with an exponential form (Touratier and Goyet, 2004b). The extension of this form to include A_T was found to further improve it (Touratier et al., 2007). The equation shown above differs slightly from that described in Touratier et al. (2007), in that it includes an additional coefficient, $f = 1\ \mu$mol kg^{-1}, to dimensionalise TrOCA^0. Note that parameters c and d respectively have units of $(^\circ C)^{-1}$ and $(\mu\text{mol kg}^{-1})^2$.

Combining Eqs. (8) and (9) creates the following expression:

$$C^{\text{TrOCA}}_{\text{ant92/95}} = \frac{\text{TrOCA} - \text{TrOCA}^0}{a} = \frac{O_2 + a\left[C_T - \frac{A_T}{2}\right] - f\exp\left(b + c\theta + \frac{d}{A_T^2}\right)}{a} \quad (10)$$

Using data collected along the WOCE I1 sections in the northern Indian Ocean, Touratier et al. (2007) optimised the values of parameters a, b, c and d. Parameter a's value (nominally 1.205 from Eqs. 1 and 5) was varied between 1.0 and 1.5, with the others optimised for each a. The best set of parameters obtained in this way was:

$a = 1.279$

$b = 7.511$

$c = -1.087 \times 10^{-2}$

$d = -7.81 \times 10^5$

($f = 1.0$)

Touratier et al. (2007) then used these values to estimate C_{ant} in the northern Indian Ocean using the following TrOCA expression:

$$C^{\text{TrOCA}}_{\text{ant}} = \frac{O_2 + 1.279\left[C_T - \frac{A_T}{2}\right]}{1.279} \quad (11)$$

$$-\frac{1.0\exp\left(7.511-(1.087\times10^{-2})\theta+\frac{-7.81\times10^{5}}{A_T^2}\right)}{1.279}$$

2.3 TrOCA and OCCAM

To examine the skill of the TrOCA method in distinguishing C_{ant} from background DIC, the method is used in a number of different ways to estimate C_{ant} from OCCAM's simulation of the industrial period. Since the simulation includes a pre-industrial DIC tracer, it is possible to separate natural and anthropogenic signals in modelled DIC, and to directly assess TrOCA's skill.

Firstly, the optimised version of the TrOCA method described in Touratier et al. (2007) is used together with output from OCCAM to estimate C_{ant} in the Indian Ocean. The performance of this same optimised version is then used with global output from OCCAM to examine its wider applicability.

Next, given that the biogeochemical model used here does not fully represent the complexity of real world biogeochemistry, it is likely that the TrOCA parameters derived from field observations are not optimal for use with our model. To this end, the TrOCA method itself is re-optimised, using output from OCCAM as input to the calibration procedure described in Touratier et al. (2007). This calibration is performed using both global, basin and regional scale subsets of the model output in order to estimate the robustness and wider utility of the optimised variants of the TrOCA method.

The skill of the resulting variants is assessed in the context of assumptions underlying the TrOCA method. This assessment takes the form of a series of further experiments to examine aspects of TrOCA such as the assumption of constant air-sea disequilibrium of CO_2 under pre-industrial and present day atmospheres, and the use of a heuristic function, Eq. (9), to approximate $TrOCA^0$.

3 Results and discussion

3.1 OCCAM simulation

Prior to using simulation output with the TrOCA method, OCCAM's performance in representing the period 1864–2004 was assessed, with particular regard to the model's carbon cycle and its simulated C_{ant} and CFC-11 distributions.

Figure 1 shows the annual average surface distribution of CFC-11 for the mid-1990s from the GLODAP climatology (Key et al., 2004) and OCCAM (see caption for further detail). While OCCAM generally captures the (primarily temperature-dependent) patterns of CFC-11 distribution, concentrations are generally elevated over those from GLODAP. This is most noticeable in the Southern Ocean, where isolines of CFC-11 are shifted up to 10° northwards. Integrating through the full water column, the GLODAP climatology estimates a total CFC-11 inventory of 0.540 Gmol, while OCCAM simulates a significantly greater uptake of 0.790 Gmol (+49%; this figure is corrected for the data gaps in the GLODAP climatology). This high oceanic inventory of CFC-11 places OCCAM near the top of the range (approximately 0.45–0.85 Gmol) of OGCMs surveyed by the OCMIP-2 project (Dutay et al., 2002; OCCAM uses the same CFC-11 protocol as the OCMIP-2 OGCMs).

Figure 2 shows vertically-integrated C_{ant} for the GLODAP climatology (Key et al., 2004) and the OCCAM simulation (see also Fig. 7 for corresponding vertical distribution). The GLODAP field shown here is an estimate of the distribution of C_{ant} based on indirect observations and the ΔC^* method (Gruber et al., 1996; Sabine et al., 2004). As such, it is an estimate based upon an alternative technique to the TrOCA method examined here. Generally, OCCAM's C_{ant} distribution is broadly in agreement with that of GLODAP, but with a number of regional discrepancies. Most notably, OCCAM estimates a much lower inventory of C_{ant} in North Atlantic Deep Water (NADW). While OCCAM still identifies this water mass as that most penetrated by C_{ant}, model concentrations are noticeably lower than in GLODAP. The waters of the Pacific basin show much greater agreement between the two estimates, though the Pacific sector of the

BGD
6, 7231–7293, 2009

Southern Ocean (and the Southern Ocean in general) shows differences. The extent of C_{ant} penetration of Southern Ocean waters is broader in OCCAM, particularly with regards to the most southern waters adjacent to Antarctica. OCCAM also estimates lower C_{ant} in the equatorial regions of both the Atlantic and Indian basins. The estimates of the GLODAP climatology in these regions are considerably more variable than in OCCAM. Nonetheless, integrating C_{ant} at the global scale finds totals of 8.66 Pmol (GLODAP) and 8.11 Pmol (OCCAM; −6.4%) in relatively close agreement.

Finally, Fig. 3 compares observational and OCCAM primary production (Behrenfeld and Falkowski, 1997; Carr et al., 2006; Westberry et al., 2008) and air-sea CO_2 flux (Takahashi et al., 2002). In terms of primary production, the model shows the greatest discrepancy with observations in the subtropics. In these regions, the model typically underestimates production in the gyre centres and shows a more pronounced "equatorial stripe" of higher productivity. The model is generally in better agreement at higher latitudes, although it underestimates productivity in the northern hemisphere (especially with respect to the VGPM model). The model shows greater agreement with observational air-sea CO_2 flux, and generally captures its zonal trends. The greatest discrepancy in this field lies in the equatorial region, where the model underestimates outgassing of CO_2 to the atmosphere.

Notwithstanding the deficiencies described above, we judged that OCCAM's performance was still adequate for it to serve as a synthetic data set for the TrOCA method.

3.2 Default TrOCA

The initial examination of TrOCA used the values of its parameters determined by Touratier et al. (2007; see Eq. 11). These values were obtained by optimising the TrOCA method with observational data from the World Ocean Circulation Experiment (WOCE) Indian Ocean I01 cruise from 1995. The resulting TrOCA method was applied to fields of OCCAM output to estimate the C_{ant} taken up by the model during its simulation of the industrial era.

Figure 4 shows observational and corresponding model fields of potential tempera-

ture, oxygen, alkalinity and DIC on an east-west section of the Indian Ocean spanning both the Arabian Sea and the Bay of Bengal. The cruise data shown here were collected between the 13th September and the 12th October 1995; the model output is the monthly average of September 1995. In general, the model replicates many of the gross features and gradients of the study region, although there are a number of significant differences. The fields of oxygen and alkalinity, for instance, do not agree with the observations within the observational error bars. This degree of mismatch is common for global models (Najjar et al., 2007) but might adversely affect the functioning of the TrOCA method given that its parameters are derived using the hydrographic data shown.

Surface potential temperatures are somewhat lower in the model, but are generally slightly elevated in the upper ocean region (above 200 m). Oxygen concentrations broadly match the pattern of saturated surface waters, a depleted midwater (200–1000 m) and moderate deep waters (below 1000 m), but the upper-midwater region of the Arabian Sea shows markedly elevated oxygen concentrations, suggesting increased ventilation of this region. Modelled alkalinity also shows deficiencies in the upper-midwater (200–600 m), but otherwise shows similar vertical gradients and captures the dipole in surface alkalinity between the Arabian Sea (high) and Bay of Bengal (low). Finally, DIC shows a similar pattern of agreement between the model and observations, again with slightly decreased model concentrations in the upper-midwater (200–600 m). Overall, while the model fields (especially oxygen and alkalinity) exhibit differences from observational fields, and which indicate deficiencies in OCCAM's hydrography, the model still captures some of the observed variability, and shows no serious systematic limitations.

Applying the TrOCA method in Eq. (11) to the tracer fields shown in Fig. 4, Fig. 5 shows TrOCA estimated C_{ant} for both observations and the model. The figure also shows the actual model C_{ant}, calculated as the difference between the historical and control DIC tracers.

All three panels concur on the placement of the highest concentrations

(>20 mmol m^{-3}) of C_{ant} in the upper 400 m of the section. They also all agree on near-zero (or below-zero in the case of both TrOCA estimates) concentrations below 1000 m. Generally, except for the surface mixed layer where back calculation techniques such as TrOCA are known to be deficient, OCCAM's simulation of C_{ant} distribution compares favourably with the observationally-based TrOCA estimate. In contrast, the TrOCA estimate of OCCAM's C_{ant} shows large discrepancies at midwater depths, particularly in the Arabian Sea where watermasses known to be almost C_{ant}-free are instead estimated to have up to 20 mmol m^{-3}. As noted above, this midwater region is also where the greatest discrepancies occur between the observational and modelled tracer fields that feed TrOCA.

Further to the regional C_{ant} estimates of Fig. 5, Fig. 6 shows the corresponding global distribution of C_{ant} estimated by the default TrOCA method. The model output used is the monthly average for September 1995, and C_{ant} is vertically integrated with only positive concentrations considered (negative concentrations are common with TrOCA, but are ignored here). The global C_{ant} total simulated is 103.1 Gt C, while the TrOCA method estimates 238.0 Gt C (or 232.4 Gt C if regions of negative concentration are included in the integral). While these totals indicate a large discrepancy between C_{ant} simulated and that estimated, the default TrOCA method does, at least on a qualitative basis, correctly identify many regions of high (e.g. northern Atlantic Ocean; Southern Ocean) and low (e.g. Indian Ocean; Arctic Sea; equatorial Atlantic Ocean) C_{ant} accumulation. However, on a quantitative basis, agreement is poor, with large overestimations in most regions where C_{ant} is identified (typically of order 50 mmol m^{-3}). In the case of C_{ant} in the Pacific Ocean, TrOCA performance is particularly poorly estimated, both qualitatively and quantitatively, with the almost C_{ant}-free equatorial region instead being evaluated as the most C_{ant}-rich region in the world.

Figure 6 also shows default TrOCA's estimate of C_{ant} based on observational fields from GLODAP (Key et al., 2004; DIC and alkalinity) and the World Ocean Atlas (Conkright et al., 2002; potential temperature, salinity and oxygen). The estimate is significantly higher (+50%) than that estimated by the ΔC^* method (155.5 Gt C against

104.0 Gt C). However, in contrast with the corresponding estimate of OCCAM C_{ant}, its distribution closely follows that of the ΔC^* method (see Fig. 2 for comparison). There are still marked deficiencies, but nothing approaching the extreme values estimated for OCCAM C_{ant} in the eastern equatorial Pacific. Figure 7 shows the corresponding vertical profiles of C_{ant}. ΔC^* and simulated OCCAM C_{ant} profiles show the greatest agreement, especially below 200 m. The default TrOCA estimate based on observational fields generally follows these, although it exhibits an anomalous midwater peak (100 m), and consistently higher deeper water concentrations (2–3 mmol m^{-3}). The TrOCA estimate based on OCCAM fields is the least congruent, with a deep (500 m) peak, and generally increasing (if still low) C_{ant} concentrations below 2000 m.

The foregoing disagreement between OCCAM simulated C_{ant} and that estimated by the default TrOCA may be due to a number of factors. Firstly, the method used was developed for a regional dataset in which particular hydrographic features are important. As described above, OCCAM's representation of this region contains a number of significant deficiencies which may interfere with the TrOCA method (e.g. ventilated midwater in the Arabian Sea). Secondly, OCCAM's biogeochemistry is a truncated and simplified representation of the real ocean systems that the TrOCA method assumes. For example, OCCAM utilises an extremely simple submodel of calcium carbonate production and dissolution that ignores known processes including saturation-dependent dissolution (e.g., Orr et al., 2005) and ballasted sinking (e.g., Armstrong et al., 2002). Thirdly, in context of the global results, the default method used was optimised using regional data, so its application to the World Ocean may be inappropriate. The values of the parameters that interrelate the ocean tracers used by TrOCA may not universally apply, especially between watermasses at different positions along the thermohaline circulation. For these reasons, in the next section we investigate optimal TrOCA parameters derived from the model output.

As a sidenote, the TrOCA method is extremely sensitive to particular changes in the input variables, and when using it care should be taken to ensure the correct form and units of these variables are used. For example: replacing potential temperature,

θ, with in situ temperature, T, increases estimated C_{ant} in the GLODAP data set to 182.1 Gt C (+17%); substituting a constant seawater density (1.026 kg l^{-1}) increases estimated C_{ant} to 170.5 Gt C (+10%). Introducing ±1% offsets to the biogeochemical tracers provides an indication of the sensitivity of the TrOCA method's C_{ant} estimates to measurement error or uncertainty: DIC, 41.7–483.8 Gt C; alkalinity, 59.7–373.2 Gt C; oxygen, 140.0–172.2 Gt C.

3.3 Optimising TrOCA

As described above, physical and biogeochemical aspects of the OCCAM simulation used here may prevent the successful application of the default TrOCA method. In this section, the optimisation approach used by Touratier et al. (2007) to tune the TrOCA method using WOCE I01 cruise data has been applied to output from the OCCAM simulation to "custom-tune" TrOCA variants. This approach aims to examine the role of different domains on the results of the TrOCA method, and to decrease the importance of particular details of OCCAM's simulated hydrography and biogeochemistry.

To examine the importance of domain size on the applicability of optimised instances of the TrOCA method, OCCAM output was divided into idealised regions at three different scales: **Global** includes the full OCCAM domain (1 region); **Basin** divides the World Ocean into Atlantic, Pacific, Indian and Southern oceans (4 regions); **Latitudinal** divides the basins into 30° bands, 90° S→60° S, 60° S→30° S, 30° S→0° N, 0° N→30° N, 30° N→60° N and 60° N→90° N. Optimisations were undertaken for all of the above, with their performance assessed both within a particular domain and at the global domain.

For each domain, appropriate OCCAM output (potential temperature, oxygen, alkalinity and DIC) was pooled from locations that satisfied either the radiocarbon ($\Delta^{14}C < -175$‰) or CFC-11 (263–271 pptv) criteria. Figure 8 shows the horizontal distribution and average depth of the resulting $\Delta^{14}C$ and CFC-11 layers. The $\Delta^{14}C$ criterion selects very old watermasses, so is confined to deep water in the Pacific and Indian oceans, and small pockets of very deep water in the well-ventilated Atlantic

and Southern oceans. In contrast, the CFC-11 criterion instead selects very young watermasses close to the ocean's surface. For the time period selected (end of northern summer), these waters are generally noticeably deeper in the water column in the northern hemisphere than in the south. Regions with strong mixing, such as the high latitudes and upwelling zones, do not have a strong CFC-11 signal to identify appropriate watermasses.

Estimated C_{ant} was calculated for the CFC-11 locations according to Eq. (8) using standard equations (Dickson and Goyet, 1994), and assuming CO_2 saturation under "pre-industrial" (288.4 ppm) and 1995 (357.4 ppm) atmospheric concentrations. Figure 9 shows the comparison between C_{ant} estimated this way and actual, OCCAM-simulated C_{ant}. In agreement with known issues with CO_2 saturation (e.g. Matsumoto and Gruber, 2005; see later), estimated C_{ant} is slightly (RMS error =3.64 mmol m^{-3}) greater than actual C_{ant}, although the discrepancy generally decreases with depth (i.e. deeper values approach the 1:1 line more closely). C_{ant} in locations satisfying the radiocarbon criterion was assumed to be at zero concentration. The resulting fields were used together with Eq. (10) to optimise the TrOCA method by minimising RMS error (using the `fminsearch` algorithm of MATLAB; Lagarias et al., 1998).

The exact procedure followed includes a small alteration from that described by Touratier et al. (2007). Their optimisation procedure involved selecting a value of parameter *a* within a defined range ($1.0<a<1.5$), and then optimising the values of parameters *b*, *c* and *d* at this value. The value of *a* that resulted in the lowest error was then selected (together with the corresponding values of *b*, *c* and *d*). In early tests using OCCAM output, we found that error minima were often not localised with the range for parameter *a* suggested (i.e. minimum error was frequently found at the lower limit of the range sampled). Consequently, rather than optimise *a* separately and constrain it, we have included it within the error optimisation process and have allowed it to adopt any value.

Table 1 shows the results of this optimisation process for each of the regions identified above. The values of the four TrOCA parameters are shown, together with the

BGD
6, 7231–7293, 2009

default TrOCA parameter values determined by Touratier et al. (2007). To assess the skill of the optimisations, each variant is then used to calculate the C_{ant} inventory for the region used to optimise it, and then the total inventory when applied to the World Ocean. The actual C_{ant} inventories for each region are also shown for comparison.

In terms of TrOCA parameter values, parameters *a* and *d* show the largest shifts from those of default TrOCA. In deriving the TrOCA method, Touratier et al. (2007) suggest a range for *a* of 1.0 to 1.5 because of its Redfieldian roots. Most optimised variants here fall within this range, though several prefer values slightly below 1.0, and one favoured a very low value of 0.288, considerably at odds with the biogeochemical relationships embodied by the parameter. In the case of parameter *d*, as well as ranging widely, optimised values also switched sign from default TrOCA. Across all of the optimised parameters, no discernible patterns emerged between the various regions (e.g. naïvely one might expect within-basin patterns because of biogeochemical gradients).

Turning to the performance of the optimised variants, as Table 1 shows, there are often very large discrepancies between actual, OCCAM simulated C_{ant} and that estimated by the variants, both at the regional and global scales. A small number of variants produce regional estimates close to that simulated, but these successes typically do not translate to the global scale. Perhaps unsurprisingly, the variants generally perform better at the regional scale at which they were optimised rather than the global scale. Excluding the variant optimised using global fields, regional estimates average at 1.595 times actual C_{ant}, while at the global scale the average is 2.290. An exception is the northernmost Atlantic region, where a significant underestimate at the regional scale translates to the best estimate at the global scale.

The C_{ant} inventories presented in Table 1 are summary statistics that omit structure and detail from the results. Figure 10 shows a pair of Taylor diagrams (Taylor, 2001) to illustrate the performance of the TrOCA variants at capturing OCCAM's actual C_{ant} distribution. These diagrams present the standard deviations (radial axis distance) and correlation coefficients (angle) of the estimated C_{ant} distributions. The standard deviations are normalised to that of actual, OCCAM simulated C_{ant}, shown by the reference

symbol at σ=1. In the case of regional fields, a number of TrOCA variants share similar variability to that of OCCAM (0.9 to 1.2), of which some southern hemisphere regions also correlate strongly (>0.9). By these measures, the worst TrOCA variant, optimised to the equatorial North Atlantic (0° N→30° N), exhibits more than twice the variability of the OCCAM C_{ant} field, and with a very poor correlation (< 0.4). At the global scale, the TrOCA variants exhibit markedly more variability, and none correlate as strongly (all are <0.9). Beyond the relative success of southern hemisphere regions at the regional scale, there are no obvious patterns or trends in the performance of the variants. Table 2 includes the values used in these figures.

Finally, Figs. 11 and 12 present graphical representations of variant TrOCA C_{ant} estimates. Figure 11 shows global zonal average C_{ant} for a selection of the TrOCA variants. While the foregoing description has generally presented single metrics of variant performance, the subplots indicate how TrOCA C_{ant} is actually distributed. A consistent feature of variants that overestimate global C_{ant} inventory is erroneously high concentrations at higher latitudes (>45°). This is frequently accompanied by unrealistic detection of C_{ant} in deep waters. Another feature poorly resolved by several variants is the relatively shallow penetration depth of C_{ant} at equatorial latitudes. Generally, models which exhibit this latter feature are separate from those with anomalous high latitude concentrations, suggesting systematic patterns of variant failure.

Figure 12 shows the global distributions of estimated C_{ant} for three cases using optimised variants. The first panel shows estimated C_{ant} using the TrOCA variant optimised using model fields with appropriate ΔC^* and CFC-11 signatures (total=262.4 Gt C). The second panel shows the same but the estimates for each basin are derived using the TrOCA variants optimised for the same basin (total=204.6 Gt C). The third panel repeats this with estimates derived using regional TrOCA variants (total=170.0 Gt C). Relative to that estimated by default TrOCA, all three panels show substantial deficiencies in their C_{ant} distributions, although there are also some small improvements. As already noted, all three panels estimate totals considerably in excess of that actually simulated, with the global panel's overestimate larger than that of default TrOCA

(238.7 Gt C). One area of improvement in all three cases is the eastern Pacific basin, where C_{ant} concentrations now more closely resemble that simulated, although they are still markedly elevated. Equatorial Atlantic concentrations of C_{ant} are also improved in the basin and regional panels, particularly the former where North Atlantic Deep Water (NADW) is correctly estimated as relatively uncontaminated with C_{ant}.

Nonetheless, despite these limited improvements, it is clear that none of the optimised TrOCA variants reliably estimates OCCAM simulated C_{ant} even at regional scales.

3.4 Bootstrapped TrOCA parameters

To estimate the variance of the optimised TrOCA parameters, a bootstrapping procedure was used with the global, basin and regional calibration datasets. Each calibration dataset was randomly resampled with replacement to produce 1000 alternative calibration datasets that were then used in optimisation.

Table 3 lists the resulting means and ranges of TrOCA parameters from the bootstrap procedure. With a small number of exceptions, the mean values recovered from the bootstrap populations are identical (to four significant figures) to those determined using the full calibration dataset. Also with a small number of exceptions, parameters *a*, *b* and *c* show narrow ranges of variability about these mean values. These variability ranges are considerably smaller than the range of parameter estimates generated between all of the regional calibration datasets, suggesting that there are robust biogeochemical differences between the regions. Parameter *d*, however, is exceptional in that its bootstrap ranges are much larger relative to bootstrap means (though still narrow relative to the optimised range of values of *d*). This, coupled to its large range of optimised values, suggests that parameter *d*, the dependence of TrOCA on alkalinity, is only weakly constrained in TrOCA.

3.5 Approximating TrOCA^0

Given Eq. (10) and the relatively good agreement between estimated and simulated C_{ant} in the calibration dataset shown in Fig. 9, the errors in estimated C_{ant} result from discrepancies in the estimates of natural, pre-industrial DIC.

Equation (6) defines the pre-industrial TrOCA tracer, TrOCA^0, as a function of oxygen, pre-industrial DIC and alkalinity. Using a calibration dataset of observations identified by $\Delta^{14}C$ and CFC-11 signatures, TrOCA^0 is appoximated with an exponential function of potential temperature and alkalinity (Eq. 9). Combining this with calculated TrOCA, this approximation forms the basis of the TrOCA method's separation of C_{ant} from DIC.

Here we use the optimised TrOCA variants to evaluate how accurate this approximation is by back-calculating estimated fields of pre-industrial DIC, C_T^0, for each variant, and comparing these with OCCAM's simulated pre-industrial DIC field. Pre-industrial DIC is estimated as follows:

$$
\begin{aligned}
C_T^{0,\,\mathrm{TrOCA}} &= C_T + \frac{\mathrm{TrOCA}^0}{a} - \frac{\mathrm{TrOCA}}{a} \\
&= C_T + \frac{f}{a}\exp\left(b + c\theta + \frac{d}{{A_T}^2}\right) - \left(\frac{O_2}{a} + C_T - \frac{A_T}{2}\right) \\
&= \frac{f}{a}\exp\left(b + c\theta + \frac{d}{{A_T}^2}\right) - \frac{O_2}{a} + \frac{A_T}{2}
\end{aligned}
\tag{12}
$$

Table 4 presents the resulting comparison between TrOCA-estimated C_T^0 and simulated C_{ant}-free DIC. Average C_T^0 estimates, and the spatial variability of these estimates, show good agreement with those simulated, and correlation between them is high (with the exception of the equatorial North Atlantic region). However, as the C_{ant}

BGD
6, 7231–7293, 2009

results already imply, RMS errors, while small relative to C_T^0, are significant relative to C_{ant}. And as cross-reference with Table 1 shows, even the lowest errors (e.g. the Southern Ocean) are still associated with large discrepancies in integrated ocean C_{ant}.

These errors are not distributed randomly within the model domain or between model variables, and Fig. 13 shows correlations between the error in C_T^0 estimates and several key TrOCA variables for the variant optimised with the full global calibration dataset. The panels show how estimated C_T^0 error varies with simulated C_{ant}, potential temperature, oxygen and alkalinity. In each case, the panels show the (logarithmic) density of OCCAM grid cells that occur over the ranges of the properties sampled. In the case of C_{ant} and potential temperature, the C_T^0 errors are distributed fairly evenly over these variables. There are small regions in which errors are focused, but the relationships are generally weak. Alkalinity similarly shows no strong relationship with C_T^0 error, although for low alkalinity values there appears to be a bias to overestimation of C_T^0 (though the total number of grid cells in this relationship is low). However, oxygen exhibits a more distinct relationship with C_T^0 error which traces out a "N"-shaped pattern in the plot. Water masses with low oxygen range in C_T^0 error from −100 to 50 mmol m^{-3}, while high oxygen water masses range −50 to 100 mmol m^{-3}, with intermediate water masses falling from 50 to −50 mmol m^{-3} as oxygen concentrations rise. This pattern is broadly repeated for other TrOCA variants as Fig. 14 shows (comparable analysis of C_T^0 error and the other TrOCA variables finds that they behave similarly across TrOCA variants; results not shown).

As noted above, this analysis finds that the errors associated with approximating C_T^0 with Eq. (12) are comparable in magnitude to the concentrations of C_{ant} found in present day seawater. Since the relatively small signal of C_{ant} is the focus of the TrOCA method, this interferes with its efficiency at deconvoluting C_{ant} from background DIC.

3.6 Estimated and actual C_{ant}

One potential source of error in the optimisation process described in the preceding section is the use of estimated C_{ant} at locations identified as possessing a peak CFC-11 signature. Estimates are based on the difference between saturation DIC concentrations under "pre-industrial" and 1995 atmospheric CO_2 concentrations. This method assumes that although DIC concentrations may change in response to the anthropogenic transient, surface disequilibrium is constant. Essentially, a given location's current DIC concentration is out of equilibrium with atmospheric pCO_2 to the same degree as it was under pre-industrial conditions.

Figure 15 shows globally averaged, surface disequilibrium for the duration of the simulation period (1864–2004). The control simulation shows the magnitude of interannual variability in disequilibrium, and the repeating cycles of this variability as the forcing data (1958–2004) is reused. While the transient simulation begins with the same disequilibrium as the control, approximately $-11\,\mathrm{mmol\,m^{-3}}$, this gradually grows, particularly after 1950, to reach a disequilibrium of around $-16.5\,\mathrm{mmol\,m^{-3}}$ by 2004 (an increase of slightly more than 50%). Consistent with Fig. 9, these results suggest that the TrOCA method's approach for estimating the C_{ant} signal in recently ventilated waters (those with the peak CFC-11 signature) may overlook a change in disequilibrium. The neglect of this increase in disequilibrium by about $5\,\mathrm{mmol\,m^{-3}}$ may explain some part of the generally too high C_{ant} values estimated by the TrOCA method.

To examine the importance of errors introduced by the estimated $C^{TrOCA}_{ant92/95}$ of Eq. (8), the TrOCA method was optimised as before, but with actual, OCCAM simulated C_{ant} substituted for estimated (or assumed zero) $C^{TrOCA}_{ant92/95}$. The global/basin/region optimisation was otherwise repeated identically using the same calibration datasets.

Table 5 and Fig. 16 (and Fig. 17) repeat earlier representations of the performance of the TrOCA variants. While the optimised values of the TrOCA parameters are not identical to those of the earlier variants, they are typically very close, and the estimated C_{ant} inventories are frequently nearly identical. Unsurprisingly, congruence is greatest

where the CFC-11 fraction of the calibration dataset is at its lowest (i.e. where near-zero C_{ant} values dominate the calibration dataset). Comparing Figs. 10 and 16 finds nearly indistinguishable performances of the actual and estimated C_{ant} variants.

3.7 C_{ant}-free calibration dataset

As described in the *Methods* section, this work makes use of an OCCAM simulation of duration 188 years (=4×47 years). However, gauged from radiocarbon measurements, the ventilation timescale of the deep ocean is up to 2000 years (Ostlund and Stuiver, 1980). As a result, the simulated ocean and carbon cycle are unlikely to be in equilibrium with one another. In particular, deep water masses identified as C_{ant}-free using $\Delta^{14}C$ are generally older than the duration of the simulation and the biogeochemical signals in them are liable to be dominated by initial conditions rather than the activity of OCCAM. As these C_{ant}-free water masses play an important role in TrOCA calibration, the preceding optimisations may be compromised by incorporating a mixture of initial conditions and simulated biogeochemistry.

To examine this potential problem, ostensibly C_{ant}-free calibration data was selected using the ventilation tracer described in the *Methods* section to identify water masses that were ventilated last during the course of the spin-up phase of the simulation (i.e. prior to the exposure of the ocean to C_{ant}). The specific age range used selected water masses of between 156 and 173 years in age. The lower age limit excluded water masses with C_{ant} concentrations of more than $2\,mmol\,m^{-3}$. The upper age limit excluded watermasses with ages within 5 years of the simulation initiation (as previously, analysis focused on September 1995 rather than the end point of the simulation). This criterion narrowed the C_{ant}-free calibration dataset from 394988 grid cells to 220810 grid cells. The resulting dataset was then used in conjunction with the CFC-11 calibration dataset to optimise the TrOCA parameters in the manner already described.

Table 6 shows the result of this procedure. As with the original optimisations, the skill of the resulting TrOCA variants is still relatively poor and extremely variable. While the new calibration dataset has generally improved the large-scale variants (3 out of 4 are

BGD
6, 7231–7293, 2009

better), the regionally-optimised variants are generally worse (8 out of 13 are worse). Considering global scale performance, the range of these optimised variants (88.2–1357.8 Gt C) is much broader than than that of the original optimised variants (93.3–461.4 Gt C), although generally the misfit with simulated C_{ant} is broadly comparable between the two optimisation efforts. The best performing variant is the same between both optimisation efforts (60° N→90° N Atlantic), and the worse performing variants are still those in the equatorial Pacific, although in all of these cases the new optimisations are worse. In terms of the estimated TrOCA parameters between the two optimisation efforts, these show weak correlations with the exception of parameter d. In the original optimised variants, this ranged widely between large positive and negative values, but here only negative values (i.e. opposite in sign from those found by Touratier et al., 2007) are estimated.

As a further test of the significance of unventilated water masses for TrOCA-estimated C_{ant}, water masses with an age greater than 173 years were excluded when C_{ant} was integrated to regional and global scales. Table 7 shows resulting C_{ant} integrals. In general, the differences are slight, indicating that the TrOCA variants are not estimating large quantities of C_{ant} in unventilated regions of the model domain. The exceptions are those variants which already massively overestimate C_{ant} (e.g. those derived using equatorial Pacific calibration data). For these variants, the figures in Table 7 differ significantly from those in Table 6, and the variant estimates significant C_{ant} where near zero occurs.

Overall, the results of this alternative optimisation suggest that filtering the calibration dataset to exclude unventilated water masses does not significantly alter the success of the optimised variants. While the use of "clean" calibration data is preferable on theoretical grounds, "contamination" of the model domain by its initial condition does not appear a major factor in the poor performance of the TrOCA variants.

4 Conclusions

Using biogeochemical tracer distributions derived from an ocean general circulation model, we have examined the ability of the TrOCA method (Touratier et al., 2007) to estimate anthropogenic carbon from a global ocean general circulation model. We find that the standard TrOCA method considerably overestimates the model's "true" anthropogenic CO_2 by about a factor of 2. Applying default TrOCA to global fields of observed ocean properties from the GLODAP and World Ocean Atlas climatologies also produces a large (about 50%) overestimate of the ocean's anthropogenic CO_2 content relative to other established methods of deconvolution (Gruber et al., 1996).

In order to test how sensitive these results are to possible deficiencies of our model, we followed the approach outlined by Touratier et al. (2007) and re-parameterised the TrOCA method utilising a range of different calibration data sets in the optimisation process. While the results showed regional differences for different calibration data sets, the overall conclusion that TrOCA tends to considerably overestimate anthropogenic CO_2 remained unchanged. Furthermore, the results of this procedure suggest that no single TrOCA parameter set can operate "universally" across the world ocean. Within the framework of our model, we also show that TrOCA's inherent assumption of similar surface pCO_2 disequilibrium in the 1990s and in the pre-industrial world is not critical.

According to our model-based analysis, the main error in the TrOCA estimates comes from the errors associated with estimating the pre-industrial value of the approximately conservative TrOCA tracer, $TrOCA^0$. Assuming no anthropogenic impact on oxygen and alkalinity, this directly corresponds to errors in the estimate of natural DIC, $C_T^{0,\,TrOCA}$ (Eq. 12). Although the relative errors of $C_T^{0,\,TrOCA}$ are small, the absolute errors are of comparable magnitude to the total anthropogenic CO_2 signal, preventing the TrOCA method from recovering C_{ant} in our OCCAM simulation.

BGD
6, 7231–7293, 2009

Appendix A

The following equations describe the tendency terms operating on the biogeochemical tracers in the model.

$$\frac{\partial P}{\partial t} = + \underbrace{[\, F_{PP}(J,\, Q_N)\, .\, P\,]}_{\text{primary production}} - \underbrace{[\, G_P\,]}_{\text{grazing loss}} - \underbrace{[\, \mu_{P1}\,]}_{\text{metabolic loss}} - \underbrace{[\, \mu_{P2}\,]}_{\text{nat. mortality}} \tag{A1}$$

$$\frac{\partial Z}{\partial t} = + \underbrace{[\, F_Z\,]}_{\text{grazing}} - \underbrace{[\, \mu_{Z1}\,]}_{\text{metabolic loss}} - \underbrace{[\, \mu_{Z2}\,]}_{\text{predation}} \tag{A2}$$

$$\frac{\partial D_N}{\partial t} = + \underbrace{[\,(1 - \beta_N)\, .\, I_N]}_{Z\text{ egestion}} + \underbrace{[\, \mu_{P2}\,]}_{P\text{ nat. mortality}} + \underbrace{[\, \mu_{Z2}\,]}_{Z\text{ predation}} - \underbrace{\left[\, \mu_{D_N}\, .\, D_N\,\right]}_{\text{remin.}} + \underbrace{[\, S(D_N)\,]}_{D\text{ sinking}} \tag{A3}$$

$$\frac{\partial N}{\partial t} = - \underbrace{[\, F_{PP}(J,\, Q_N)\, .\, P\,]}_{\text{primary production}} + \underbrace{[\, E_Z\,]}_{Z\text{ excretion}} + \underbrace{[\, \phi\, .\, G_P\,]}_{\text{messy feeding}} + \underbrace{[\, \mu_{P1}\,]}_{P\text{ metab. loss}} + \underbrace{[\, \mu_{Z1}\,]}_{Z\text{ metab. loss}} + \underbrace{\left[\, \mu_{D_N}\,\right]}_{D\text{ remin.}} \tag{A4}$$

$$\frac{\partial D_C}{\partial t} = + \underbrace{[\,(1 - \beta_C)\, .\, I_C]}_{Z\text{ egestion}} + \underbrace{[\, \theta_P\, .\, \mu_{P2}\,]}_{P\text{ nat. mortality}} + \underbrace{[\, \theta_Z\, .\, \mu_{Z2}\,]}_{Z\text{ predation}} - \underbrace{\left[\, \mu_{D_C}\,\right]}_{\text{remin.}} + \underbrace{[\, S(D_C)\,]}_{D\text{ sinking}} \tag{A5}$$

BGD
6, 7231–7293, 2009

$$\frac{\partial DIC}{\partial t} = -\underbrace{[\,F_{PP}(J,\,Q_N)\,.\,\theta_P\,.\,P\,]}_{\text{organic production}} - \underbrace{[\,F_{Ca}\,.\,F_{PP}(J,\,Q_N)\,.\,\theta_P\,.\,P\,]}_{\text{inorganic production}} \tag{A6}$$
$$+ \underbrace{[\,R_Z\,]}_{Z\text{ respiration}} + \underbrace{[\,\phi\,.\,\theta_P\,.\,G_P\,]}_{\text{messy feeding}} + \underbrace{[\,\theta_P\,.\,\mu_{P1}\,]}_{P\text{ metab. loss}} + \underbrace{[\,\theta_Z\,.\,\mu_{Z1}\,]}_{Z\text{ metab. loss}}$$
$$+ \underbrace{[\,\mu_{D_C}\,]}_{D\text{ remin}} + \underbrace{[\,R_{Ca}(k)\,.\,T_{Ca}\,]}_{\text{inorganic remin.}} + \underbrace{[\,F_{\text{atm},C}\,]}_{\text{air–sea flux}}$$

$$\frac{\partial ALK}{\partial t} = -\underbrace{[\,2\,.\,F_{Ca}\,.\,F_{PP}(J,\,Q_N)\,.\,\theta_P\,.\,P\,]}_{\text{inorganic production}} + \underbrace{[\,R_{Ca}(k)\,.\,2\,.\,T_{Ca}\,]}_{\text{inorganic remin.}} \tag{A7}$$

$$\frac{\partial O_2}{\partial t} = +\underbrace{[\,\theta_{\text{phy}}\,.\,F_{PP}(J,\,Q_N)\,.\,P\,]}_{\text{primary production}} - \underbrace{[\,\theta_{\text{phy}}\,.\,\phi\,.\,G_P\,]}_{\text{messy feeding}} \tag{A8}$$
$$- \underbrace{[\,\theta_{\text{nit}}\,.\,E_Z\,]}_{Z\text{ excretion}} - \underbrace{[\,\theta_{\text{rem}}\,.\,R_Z\,]}_{Z\text{ respiration}} - \underbrace{[\,\theta_{\text{phy}}\,.\,\mu_{P1}\,]}_{P\text{ metab. loss}} - \underbrace{[\,\theta_{\text{zoo}}\,.\,\mu_{Z1}\,]}_{Z\text{ metab. loss}}$$
$$- \underbrace{[\,\theta_{\text{nit}}\,.\,\mu_{D_N}\,]}_{D_N\text{ remin}} - \underbrace{[\,\theta_{\text{rem}}\,.\,\mu_{D_C}\,]}_{D_C\text{ remin}} + \underbrace{[\,F_{\text{atm},O_2}\,]}_{\text{air–sea flux}}$$

where,

$$J(k) = \int_{z_k}^{z_{k+1}} F(I_{z_k}\,.\,\exp\{-(k_w + (k_c\,.\,P(k)))\,.\,z\})\,dz \tag{A9}$$

$$F_I = \frac{(V_t\,.\,\alpha\,.\,I)}{\sqrt{(V_t^2 + (\alpha^2\,.\,I^2))}} \tag{A10}$$

$$V_t = V_p\,.\,1.066^T \tag{A11}$$

BGD
6, 7231–7293, 2009

$$Q_N = \frac{N}{k_N + N} \quad \text{(A12)}$$

$$F_{PP}(J, Q_N) = \min(J, V_t \cdot Q_N) \quad \text{(A13)}$$

$$G_P = \frac{g \cdot k_g P^2 \cdot Z}{g + (k_g \cdot P^2)} \quad \text{(A14)}$$

$$\mu_{P1} = \phi_{P1} \cdot P \quad \text{(A15)}$$

$$\mu_{P2} = \phi_{P2} \cdot P^2 \quad \text{(A16)}$$

$$I_N = (1 - \phi) \cdot G_P \quad \text{(A17)}$$

$$I_C = (1 - \phi) \cdot (\theta_P \cdot G_P) \quad \text{(A18)}$$

$$\theta_F = \frac{I_C}{I_N} \quad \text{(A19)}$$

$$F_Z = \frac{\beta_C \cdot k_C \cdot I_C}{\theta_Z} \quad \text{(A20)}$$

$$E_Z = I_C \cdot \left(\frac{\beta_N}{\theta_F} - \frac{\beta_C \cdot k_C}{\theta_Z} \right) \quad \text{(A21)}$$

$$R_Z = (\beta_C \cdot I_C) - (\theta_Z \cdot F_Z) \quad \text{(A22)}$$

$$\mu_{Z1} = \phi_{Z1} \cdot Z \quad \text{(A23)}$$

$$\mu_{Z1} = \phi_{Z2} \cdot Z^2 \quad \text{(A24)}$$

$$\mu_{D_N} = \mu_D \cdot D_N \quad \text{(A25)}$$

$$\mu_{D_C} = \mu_{D_C} \cdot D_C \quad \text{(A26)}$$

$$F_{Ca} = \text{Fixed fraction of primary production} \quad \text{(A27)}$$

$$T_{Ca} = \int_{k=1}^{k=66} F_{Ca} \cdot F_{PP}(J, Q_N) \cdot \theta_P \cdot P \quad \text{(A28)}$$

$$f_{Ca}(k) = \exp(-\frac{z(k) - z_{Ca}}{d_{Ca}}) \quad \text{(A29)}$$

BGD
6, 7231–7293, 2009

$$R_{Ca}(k) = f_{Ca}(k-1) - f_{Ca}(k) \quad \text{(A30)}$$

$$\theta_{\text{phy}} = \frac{32}{16} + \left(\theta_P \cdot \frac{119}{106}\right) \quad \text{(A31)}$$

$$\theta_{\text{zoo}} = \frac{32}{16} + \left(\theta_Z \cdot \frac{119}{106}\right) \quad \text{(A32)}$$

$$\theta_{\text{nit}} = \frac{32}{16} \quad \text{(A33)}$$

$$\theta_{\text{rem}} = \frac{119}{106} \quad \text{(A34)}$$

$$V_z = V_0 + (0.02 \cdot z) \quad \text{(A35)}$$

where,

	Phytoplankton		
V_p	Maximum growth rate (at 0°C)	0.6	d^{-1}
α	Initial slope of P-I curve	0.025	$(W\ m^{-2})^{-1}\ d^{-1}$
k_w	Background attenuation coefficient	0.04	m^{-1}
k_c	Phytoplankton self-shading coefficent	0.03	$m^{-1}\ (mmol\ N\ m^{-3})^{-1}$
K_N	DIN uptake half-saturation concentration	0.5	$mmol\ N\ m^{-3}$
ϕ_{P1}	Density-independent loss rate	0.05	d^{-1}
ϕ_{P2}	Density-dependent loss rate	0.05	$d^{-1}\ (mmol\ N\ m^{-3})^{-1}$
F_{Ca}	$CaCO_3$ fraction of total primary production	0.01	–
θ_P	C:N ratio	6.625	$mol\ C\ (mol\ N)^{-1}$

BGD
6, 7231–7293, 2009

	Zooplankton		
g	Maximum grazing rate	2.0	d^{-1}
k_g	Prey capture rate	1.0	m^6 (mmol N)$^{-2}$ d^{-1}
β_N	N assimilation efficiency	0.77	–
β_C	C assimilation efficiency	0.64	–
k_C	Net C growth efficiency	0.80	–
ϕ	Grazing inefficiency (messy feeding)	0.23	–
ϕ_{Z1}	Density-independent loss rate	0.03	d^{-1}
ϕ_{Z2}	Density-dependent loss rate	0.20	d^{-1} (mmol N m^{-3})$^{-1}$
θ_Z	C:N ratio	5.625	mol C (mol N)$^{-1}$

	Other parameters		
μ_D	Detrital N remineralisation rate	0.01	d^{-1}
μ_{D_C}	Detrital C remineralisation rate	0.008	d^{-1}
$V_{\min}$	Detrital sinking speed at 0 m	3.5	m d^{-1}
z_{Ca}	Minimum $CaCO_3$ dissolution depth	127	m
d_{Ca}	$CaCO_3$ dissolution e-folding length scale	3500	m
$O_{\min}$	Aerobic remineralisation O_2 minimum	4.0	mmol O_2 m^{-3}
θ_{phy}	Oxygen evolution/consumption via P	9.4375	mol O_2 (mol N)$^{-1}$
θ_{zoo}	Oxygen consumption via Z	8.3149	mol O_2 (mol N)$^{-1}$
θ_{rem}	Oxygen consumption by C remineralisation	1.1226	mol O_2 (mol C)$^{-1}$
θ_{nit}	Oxygen consumption by N nitrification	2.0	mol O_2 (mol N)$^{-1}$

Acknowledgements. The authors would like to thank Bablu Sinha, Beverly de Cuevas and Andrew Coward for technical assistance with OCCAM; Catherine Goyet and Franck Touratier for assistance with the TrOCA method; Adrian Martin for advice and assistance concerning bootstrap optimisation; Robert O'Malley for providing observational primary production estimates; and Peter Brown, Marta Álvarez and Elaine McDonagh for general discussions of the TrOCA method. The authors are also grateful to the WOCE community for making their observational archive both available and easily accessible. AY is funded on a UK National Environment Re-

search Council (NERC) standard grant (NE/C00387X/1). The authors declare that they have no competing interests.

References

Älvarez, M., Lo Monaco, C., Tanhua, T., Yool, A., Oschlies, A., Bullister, J. L., Goyet, C., Metzl, N., Touratier, F., McDonagh, E., and Bryden, H. L.: Estimating the storage of anthropogenic carbon in the subtropical Indian Ocean: a comparison of five different approaches, Biogeosciences, 6, 681–703, 2009, http://www.biogeosciences.net/6/681/2009/. 7234

Anderson, L. A.: On the hydrogen and oxygen content of marine phytoplankton, Deep-Sea Res. I, 42, 1675–1680, 1995. 7236

Anderson, T. R. and Pondaven, P.: Non-redfield carbon and nitrogen cycling in the Sargasso Sea: pelagic imbalances and export flux, Deep-Sea Res. I, 50, 573–591, 2003. 7236

Archer, D.: Fate of fossil fuel CO_2 in geologic time. J. Geophys. Res., 110, C09S05, doi:10.1029/2004JC002625, 2005. 7233

Armstrong, R. A., Lee, C., Hedges, J. I., Honjo, S., and Wakeham, S. G.: A new, mechanistic model for organic carbon fluxes in the ocean: based on the quantitative association of POC with ballast minerals, Deep-Sea Res. II, 49, 219–236, 2002. 7247

Behrenfeld, M. J. and Falkowski, P. G.: Photosynthetic rates derived from satellite-based chlorophyll concentration, Limnol. Oceanogr., 42, 1–20, 1997. 7244

Brewer, P. G.: Direct observations of the oceanic CO_2 increase, Geophys. Res. Lett., 5, 997–1000, 1978. 7233, 7239

Brewer, P. G., Friederich, G., Peltzer, E. T. and Orr Jr., F. M.: Direct experiments on the ocean disposal of fossil fuel CO_2, Science, 284, 943–945, 1999.

Carr, M.-E., Friedrichs, M. A. M., Schmeltz, M. et al.: A comparison of global estimates of marine primary production from ocean color, Deep-Sea Res. II, 53, 741–770, 2006. 7244

Chen, G.-T. and Millero, F. J.: Gradual increase of oceanic carbon dioxide, Nature, 277, 205–206, 1979. 7233

Chen, C.-T. A. and Pytkowicz, R. M.: On the total CO_2-titration alkalinity-oxygen system in the Pacific Ocean, Nature, 281, 362–365, 1979. 7233

Conkright, M. E., Antonov, J. I., Baranova, O. et al.: World Ocean Database 2001, Volume 1:

Introduction (ed. Sydney Levitus), NOAA Atlas NESDIS 42, US Government Printing Office, Washington, D.C., USA, 2002. 7237, 7246

Dickson, A. G. and Goyet, C.: Handbook of methods for the analysis of the various parameters of the carbon dioxide system in sea water; version 2. US Department of Energy, ORNL/CDIAC-74, 1994. 7249

Dutay, J.-C., Bullister, J. L., Doney, S.C. et al.: Evaluation of ocean model ventilation with CFC-11: comparison of 13 global ocean models, Ocean Modelling, 4, 89–120, 2002. 7243

Fallon, S. J., Guilderson, T. P., and Caldeira, K.: Carbon isotope constraints on vertical mixing and air-sea CO_2 exchange, Geophys. Res. Lett., 30, 2289, doi:10.1029/2003GL018049, 2003. 7233

Friedlingstein, P., Cox, P., Betts, R. et al.: Climate-Carbon Cycle Feedback Analysis: Results from the C^4MIP Model Intercomparison, J. Climate, 19, 3337–3353, 2006. 7233

Gerber, M., Joos, F., Vázquez-Rodríguez, M., Touratier, F., and Goyet, C.: Regional air-sea fluxes of anthropogenic carbon inferred with an Ensemble Kalman Filter, Global Biogeochem. Cycles, 23, GB1013, doi:10.1029/2008GB003247, 2009. 7234

Glessmer, M. S., Oschlies, A., and Yool, A.: Simulated impact of double-diffusive mixing on physical and biogeochemical upper ocean properties, J. Geophys. Res., 113, C08029, doi:10.1029/2007JC004455, 2008. 7237

Goyet, C. and Brewer, P. G.: Biochemical properties of the oceanic carbon cycle, Modelling Oceanic Climate Interactions, NATO ASI Series, I 11, edited by: Willebrand, J. and Anderson, D. L. T., 271–297, 1993. 7234

Gruber, N.: Anthropogenic CO_2 in the Atlantic Ocean, Global Biogeochem. Cy., 12, 165–191, 1998. 7234

Gruber, N., Sarmiento, J. L., and Stocker, T. F.: An improved method for detecting anthropogenic CO_2 in the oceans, Global Biogeochem. Cycles, 10, 809–837, 1996. 7234, 7243, 7258

Key, R. M., Kozyr, A., Sabine, C. L. et al.: A global ocean carbon climatology: Results from Global Data Analysis Project (GLODAP), Global Biogeochem. Cy., 18, GB4031, doi:10.1029/2004GB002247, 2004. 7234, 7237, 7243, 7246

Lagarias, J. C., Reeds, J. A., Wright, M. H., and Wright, P. E.: Convergence properties of the Nelder-Mead simplex method in low dimensions, SIAM J. Optimization, 9, 112–147, 1998. 7249

Large, W. and Yeager, S.: Diurnal to decadal global forcing for ocean and sea-ice models:

the data sets and flux climatologies. CGD Division of the National Center for Atmospheric Research, NCAR Technical Note: NCAR/TN-460+STR, 2004. 7236

Lo Monaco, C., Metzl, N., Poisson, A., Brunet, C., and Schauer, B.: Anthropogenic CO_2 in the Southern Ocean: Distribution and inventory at the Indian-Atlantic boundary (World Ocean Circulation Experiment line I6), J. Geophs. Res., 110, C06010, doi:10.1029/2004JC002643, 2005. 7234

Manning, A. C. and Keeling, R. F.: Global oceanic and land biotic carbon sinks from the Scripps atmospheric oxygen flask sampling network, Tellus, 58B, 95–116, 2006. 7239

Marsh, R., de Cuevas, B. A., Coward, A. C., Bryden, H. L., and Alvarez, M.: Thermohaline circulation at three key sections of the North Atlantic over 1985–2002, Geophys. Res. Lett., 32, L10604, doi:10.1029/2004GL022281, 2005. 7235

Matsumoto, K. and Gruber, N.: How accurate is the estimation of anthropogenic carbon in the ocean? An evaluation of the ΔC^* method, Global Biogeochem. Cy., 19, GB3014, doi:10.1029/2004GB002397, 2005. 7234, 7249

Najjar, R. G. and Orr, J. C.: Biotic-HOWTO. OCMIP-2 Project, 15 (http://www.ipsl.jussieu.fr/OCMIP/), 1999. 7236

Najjar, R. G., Jin, X., Louanchi, F. et al.: Impact of circulation on export production, dissolved organic matter, and dissolved oxygen in the ocean: Results from Phase II of the Ocean Carbon-cycle Model Intercomparison Project (OCMIP-2), Global Biogeochem. Cy., 21, GB3007, doi:10.1029/ 2006GB002857, 2007. 7236, 7245

Orr, J., Dutay, J.-C., Najjar, R., Bullister, J., and Brockmann, P.: CFC-HOWTO. OCMIP-2 Project, 12 pp., (http://www.ipsl.jussieu.fr/OCMIP/), 1999. 7237

Orr, J., Najjar, J., Sabine, C., and Joos, F.: Abiotic-HOWTO. OCMIP-2 Project, 29 pp. (http://www.ipsl.jussieu.fr/OCMIP/), 1999. 7236, 7237

Orr, J. C., Fabry, V. J., Aumont, O. et al.: Anthropogenic ocean acidification over the twenty-first century and its impact on calcifying organisms, Nature, 437, 681–686, 2005. 7233, 7247

Oschlies, A.: Model-derived estimates of new production: New results point towards lower values, Deep-Sea Res. II, 48, 2173–2197, 2001. 7236

Östlund, G. and Stuiver, M.: GEOSECS Pacific radiocarbon, Radiocarbon, 22, 25–53, 1980. 7256

Palmer, J. R. and Totterdell, I. J.: Production and export in a global ocean ecosystem model, Deep-Sea Res. I, 48, 1169–1198, 2001. 7236

Papaud, A. and Poisson, A.: Distribution of dissolved CO_2 in the Red Sea and correlation with

other geochemical tracers, J. Mar. Res., 44, 385–402, 1986. 7233
Pérez, F. F., Álvarez, M., and Ríos, A. F.: Improvements on the back-calculation technique for estimating anthropogenic CO_2, Deep-Sea Res. I, 49, 859–875, 2002. 7234
Raven, J. A. and Falkowski, P. G.: Oceanic sinks for atmospheric CO_2, Plant Cell Environ., 22, 741–755, 1999.
Revelle, R. and Seuss, H. E.: Carbon Dioxide Exchange between Atmosphere and Ocean and the Question of an Increase of Atmospheric CO_2 During the Past Decades, Tellus, 9, 18–27, 1957. 7233
Sabine, C. L., Key, R. M., Johnson, K. M., Millero, F. J., Poisson, A., Sarmiento, J. L., Wallace, D. W. R., and Winn, C. D.: Anthropogenic CO_2 inventory of the Indian Ocean, Global Biogeochem. Cy., 13, 179–198, 1999. 7234
Sabine, C. L., Feely, R. A., Key, R. M., Bullister, J. L., Millero, F. J., Lee, K., Peng, T. H., Tilbrook, B., Ono, T., and Wong, C. S.: Distribution of anthropogenic CO_2 in the Pacific Ocean, Global Biogeochem. Cycles, 16, GB1083, 2002. 7234
Sabine, C. L., Feely, R. A., Gruber, N., Key, R. M., Lee, K., Bullister, J. L., Wanninkhof, R., Wong, C. S., Wallace, D. W. R., Tilbrook, B., Millero, F. J., Peng, T.-H., Kozyr, A., Ono, T., and Rios, A. F.: The oceanic sink for anthropogenic CO_2, Science, 305, 367–371, 2004. 7243
Sandrini, S., Ait-Ameur, N., Rivaro, P., Massolo, S., Touratier, F., Tositti, L., and Goyet, C.: Anthropogenic carbon distribution in the Ross Sea, Antarctica, Antarct. Sci., 19, 395–407, 2007. 7234
Sarmiento, J. and Gruber, N.: Ocean Biogeochemical Dynamics. Princeton University Press, New Jersey, USA, 2006.
Schmittner, A., Oschlies, A., Giraud, X., Eby, M., and Simmons, H. L.: A global model of the marine ecosystem for long-term simulations: Sensitivity to ocean mixing, buoyancy forcing, particle sinking, and dissolved organic matter cycling, Global Biogeochem. Cy., 19, GB3004, doi:10.1029/2004GB002283, 2005. 7236
Sinha, B. and Yool, A.: Extension of the OCCAM 1° ocean general circulation model to include the biogeochemical cycles of carbon and oxygen, Part I: Technical description. National Oceanography Centre, Southampton, Research and Consultancy Report No. 5, 81 pp. (unpublished manuscript), 2006. 7236
Sonnerup, R. E., McNichol, A. P., Quay, P. D., Gammon, R. H ., Bullister, J. L., Sabine, C. L., and Slater, R. D.: Anthropogenic $\delta^{13}C$ changes in the North Pacific Ocean reconstructed using a multiparameter mixing approach (MIX), Tellus B, 59, 303–317, 2007. 7233

Takahashi, T., Sutherland, S. C., Sweeney, C. et al.: Global sea-air CO_2 flux based on climatological surface ocean pCO_2, and seasonal biological and temperature effects, Deep-Sea Res. II, 49, 1601–1622, 2002. 7244

Taylor, K. E.: Summarizing multiple aspects of model performance in a single diagram, J. Geophys. Res., 106, 7183–7192, 2001. 7250

Touratier, F. and Goyet, C.: Definition, properties, and Atlantic Ocean distribution of the new tracer TrOCA, J. Mar. Sys., 46, 169–179, 2004. 7234, 7238, 7240

Touratier, F. and Goyet, C.: Applying the new TrOCA approach to assess the distribution of anthropogenic CO2 in the Atlantic Ocean, J. Mar. Sys., 46, 181–197, 2004. 7234, 7241

Touratier, F., Goyet, C., Coatanoan, C., and Andrie, C.: Assessments of anthropogenic CO_2 distribution in the tropical Atlantic Ocean, Deep-Sea Res. I, 52, 2275–2284, 2005. 7234

Touratier, F., Azouzi, L., and Goyet, C.: CFC-11, $\Delta^{14}C$ and ^3H tracers as a means to assess anthropogenic CO_2 concentrations in the ocean, Tellus B, 59, 318–325, 2007. 7234, 7238, 7240, 7241, 7242, 7244, 7248, 7249, 7250, 7257, 7258

Tsunogai, S., Ono, T., and Watanabe, S.: Increase in total carbonate in the Western North Pacific water and a hypothesis on the missing sink of anthropogenic carbon, J. Oceanogr., 49, 305–315, 1993. 7234

Walker, S. J., Weiss, R. F. and Salameh, P. K.: Reconstructed histories of the annual mean atmospheric mole fractions for the halocarbons CFC-11, CFC-12, CFC-113 and carbon tetrachloride, J. Geophys. Res., 105, 14285–14296, 2000. 7237

Warner, M. J. and Weiss, R. F.: Solubilities of chlorofluorocarbons 11 and 12 in water and sea water, Deep-Sea Res., 32, 1485–1497, 1985. 7237, 7240

Westberry, T., Behrenfeld, M. J., Siegel, D. A., and Boss, E.: Carbon-based primary productivity modeling with vertically resolved photoacclimation, Global Biogeochem. Cy., 22, GB2024, doi:10.1029/2007GB003078, 2008. 7244

Yool, A. and Sinha, B.: Extension of the OCCAM 1° ocean general circulation model to include the biogeochemical cycles of carbon and oxygen, Part II: Initial Experiments, National Oceanography Centre, Southampton, Research and Consultancy Report No. 6, 159 pp. (unpublished manuscript), 2006. 7236

Yool, A., Martin, A. P., Fernández, C., and Clark, D. R.: The significance of nitrification for oceanic new production, Nature, 447, 999–1002, 2007. 7237

Yool, A., Shepherd, J. G., Bryden, H. L., and Oschlies, A.: Low efficiency of nutrient translocation for enhancing oceanic uptake of carbon dioxide, J. Geophys. Res., in press, 2009.

7237
Zheng, M., DeBruyn, W. J., and Saltzman, E. S.: Measurements of the diffusion coefficients of CFC-11 and CFC-12 in pure water and seawater, J. Geophys. Res., 103, 1375–1379, 1998. 7237

Table 1. TrOCA optimisation using estimated C_{ant} at peak CFC-11 locations. Optimised values of TrOCA parameters *a*, *b*, *c* and *d* are shown for a range of geographical domains, together with the regional and global C_{ant} inventories that result from their use. The table also includes the corresponding actual C_{ant} simulated by OCCAM. C_{ant} inventories are in Gt C, with negative values of TrOCA estimates set to zero.

Domain		TrOCA parameters				C_{ant} inventory		
		a	*b*	*c*	*d*	Regional		Global
				$\times 10^{-2}$	$\times 10^{5}$	TrOCA	Actual	TrOCA
Default TrOCA		*1.279*	*7.511*	*−1.087*	*7.810*	–	–	*232.4*
World Ocean		0.967	7.044	−1.003	4.443	262.4	103.5	262.4
Atlantic Ocean		1.192	7.478	−1.084	−9.014	40.7	33.9	152.6
Pacific Ocean		0.946	6.969	−1.010	7.581	118.3	48.4	265.1
Indian Ocean		1.211	7.398	−1.107	−4.159	38.5	21.3	226.8
Atlantic	(60° N→90° N)	0.716	7.113	−1.416	−8.438	1.3	2.7	93.3
	(30° N→60° N)	1.072	7.374	−1.129	−7.820	11.6	10.5	134.4
	(0° N→30° N)	0.288	6.477	−1.077	−7.774	10.1	6.7	280.3
	(30° S→0° N)	0.999	7.417	−1.041	−14.147	9.9	4.2	218.8
	(60° S→30° S)	1.328	7.468	−1.144	−3.081	8.4	8.3	144.4
Pacific	(30° N→60° N)	1.146	7.230	−1.192	2.945	9.5	5.9	165.2
	(0° N→30° N)	0.904	6.881	−1.049	10.294	28.4	9.8	320.0
	(30° S→0° N)	0.811	6.892	−0.893	3.907	29.2	11.8	461.4
	(60° S→30° S)	1.030	7.072	−1.087	6.330	31.9	17.9	187.7
Indian	(0° N→30° N)	1.101	7.427	−0.988	−11.217	3.0	2.0	429.1
	(30° S→0° N)	1.267	7.441	−1.131	−4.205	11.3	8.2	224.5
	(60° S→30° S)	1.322	7.292	−1.179	6.469	10.5	10.3	184.9
Southern	(90° S→60° S)	1.274	7.384	−1.391	−0.486	4.8	5.2	304.0

BGD
6, 7231–7293, 2009

Table 2. Estimated C_{ant} statistics (mean, standard deviation, RMS error and correlation coefficient) for TrOCA variants optimised using regional calibration datasets (est. columns). The statistics are calculated for the same optimisation regions. Corresponding statistics for the actual, OCCAM-simulated C_{ant} are also shown (act. columns). Optimisations here make use of estimated C_{ant} at CFC-11 locations. Negative C_{ant} estimates set to zero prior to statistic calculation.

Domain		Mean C_{ant} Est.	Mean C_{ant} Act.	St. dev. C_{ant} Est.	St. dev. C_{ant} Act.	RMS error	Correl. coeff.	Calibration data Samples	Calibration data CFC frac.
		mmol m^{-3}		mmol m^{-3}		mmol m^{-3}	–	#	–
World Ocean		16.485	6.504	19.800	11.931	16.820	0.743	394988	0.164
Atlantic Ocean		9.624	8.008	14.901	11.848	7.080	0.892	19069	0.852
Pacific Ocean		13.474	5.509	18.841	11.566	15.491	0.716	312067	0.124
Indian Ocean		13.233	7.318	17.504	12.814	10.143	0.898	63852	0.153
Atlantic	(60° N→90° N)	5.457	11.423	12.188	12.902	11.861	0.667	797	1.000
	(30° N→60° N)	16.426	14.826	18.075	13.179	9.408	0.870	1502	0.978
	(0° N→30° N)	9.388	6.213	25.424	11.255	24.141	0.350	3393	1.000
	(30° S→0° N)	10.397	4.456	10.778	10.324	9.684	0.738	7796	0.939
	(60° S→30° S)	8.348	8.191	13.804	11.292	3.655	0.977	5571	0.586
Pacific	(30° N→60° N)	7.494	4.633	14.566	10.812	10.085	0.748	62184	0.046
	(0° N→30° N)	10.334	3.566	14.652	10.023	13.769	0.583	109912	0.088
	(30° S→0° N)	12.776	5.180	16.694	11.744	14.773	0.653	98293	0.249
	(60° S→30° S)	15.766	8.838	21.482	13.290	12.708	0.919	39676	0.047
Indian	(0° N→30° N)	6.906	4.489	12.034	10.383	8.278	0.760	15170	0.119
	(30° S→0° N)	9.103	6.595	14.275	13.278	5.517	0.939	39302	0.182
	(60° S→30° S)	9.775	9.632	15.325	13.222	3.536	0.980	9152	0.093
Southern	(90° S→60° S)	5.655	6.137	9.220	8.957	4.286	0.891	2240	0.000

BGD
6, 7231–7293, 2009

Table 3. The results from bootstrap optimisation of TrOCA using estimated C_{ant} at peak CFC-11 locations. Mean (left columns) and range (right columns) values of TrOCA parameters *a*, *b*, *c* and *d* are shown for a range of geographical domains. Range here is the width of the distribution that encompasses the region 5% to 95% of the optimised parameters.

Domain		TrOCA parameters							
		Mean	Range	Mean	Range	Mean	Range	Mean	Range
		a		*b*		$c \times 10^{-2}$		$d \times 10^{5}$	
World Ocean		0.967	0.004	7.044	0.009	−1.003	0.003	4.436	0.410
Atlantic Ocean		1.192	0.010	7.478	0.011	−1.084	0.003	−9.015	0.321
Pacific Ocean		0.946	0.005	6.969	0.008	−1.010	0.002	7.576	0.251
Indian Ocean		1.211	0.009	7.398	0.012	−1.107	0.003	−4.158	0.461
Atlantic	(60° N→90° N)	0.714	0.216	7.108	0.237	−1.420	0.132	−8.418	1.938
	(30° N→60° N)	1.071	0.082	7.374	0.073	−1.129	0.020	−7.837	1.167
	(0° N→30° N)	0.162	0.090	6.188	0.235	−1.193	0.121	−5.047	2.980
	(30° S→0° N)	0.999	0.022	7.417	0.020	−1.041	0.005	−14.146	0.237
	(60° S→30° S)	1.327	0.105	7.466	0.161	−1.144	0.028	−3.027	5.001
Pacific	(30° N→60° N)	1.146	0.003	7.230	0.010	−1.192	0.015	2.947	0.606
	(0° N→30° N)	0.904	0.008	6.881	0.011	−1.049	0.007	10.290	0.514
	(30° S→0° N)	0.811	0.007	6.892	0.011	−0.893	0.005	3.906	0.414
	(60° S→30° S)	1.030	0.039	7.072	0.074	−1.087	0.014	6.337	2.287
Indian	(0° N→30° N)	1.101	0.013	7.427	0.010	−0.988	0.007	−11.217	0.382
	(30° S→0° N)	1.267	0.003	7.441	0.005	−1.131	0.003	−4.205	0.304
	(60° S→30° S)	1.322	0.011	7.292	0.018	−1.179	0.008	6.458	0.635
Southern	(90° S→60° S)	1.274	0.002	7.386	0.048	−1.387	0.075	−0.625	2.623

Table 4. Estimated C_T^0 statistics (mean, standard deviation, RMS error and correlation coefficient) for TrOCA variants optimised using regional calibration datasets (est. columns). The statistics are calculated for the same optimisation regions. Corresponding statistics for the actual, OCCAM-simulated C_T^0 are also shown (act. columns).

Domain		Mean C_T^0		St. dev. C_T^0		RMS	Correl.
		Est.	Act.	Est.	Act.	error	coeff.
		mol m^{-3}		mol m^{-3}		mol m^{-3}	–
World Ocean		2.301	2.308	0.115	0.106	0.032	0.963
Atlantic Ocean		2.240	2.240	0.066	0.065	0.009	0.990
Pacific Ocean		2.340	2.344	0.115	0.109	0.018	0.988
Indian Ocean		2.292	2.297	0.098	0.094	0.010	0.997
Atlantic	(60° N→90° N)	2.225	2.172	0.079	0.053	0.064	0.932
	(30° N→60° N)	2.202	2.201	0.074	0.067	0.011	0.994
	(0° N→30° N)	2.334	2.232	0.151	0.059	0.153	0.745
	(30° S→0° N)	2.255	2.258	0.059	0.055	0.012	0.981
	(60° S→30° S)	2.264	2.263	0.062	0.059	0.005	0.998
Pacific	(30° N→60° N)	2.379	2.380	0.117	0.115	0.011	0.996
	(0° N→30° N)	2.374	2.374	0.109	0.106	0.019	0.984
	(30° S→0° N)	2.346	2.348	0.115	0.111	0.020	0.986
	(60° S→30° S)	2.283	2.289	0.095	0.088	0.013	0.995
Indian	(0° N→30° N)	2.352	2.353	0.100	0.100	0.009	0.996
	(30° S→0° N)	2.302	2.304	0.103	0.101	0.006	0.999
	(60° S→30° S)	2.268	2.267	0.077	0.075	0.004	0.999
Southern	(90° S→60° S)	2.289	2.288	0.039	0.040	0.004	0.994

Table 5. As Table 1 except TrOCA optimisation using actual C_{ant} at peak CFC-11 locations. Optimised values of TrOCA parameters *a*, *b*, *c* and *d* are shown for a range of geographical domains, together with the regional and global C_{ant} inventories that result from their use. The table also includes the corresponding actual C_{ant} simulated by OCCAM. C_{ant} inventories are in Gt C, with negative values of TrOCA estimates set to zero.

Domain		TrOCA parameters				C_{ant} inventory		
		a	*b*	*c*	*d*	Regional		Global
				$\times 10^{-2}$	$\times 10^{5}$	TrOCA	Actual	TrOCA
Default TrOCA		*1.279*	*7.511*	*–1.087*	*7.810*	–	–	*232.4*
World Ocean		0.971	7.059	–0.992	3.771	262.3	103.5	262.3
Atlantic Ocean		1.130	7.417	–1.058	–8.199	40.4	33.9	151.4
Pacific Ocean		0.950	6.987	–0.997	6.776	118.3	48.4	265.1
Indian Ocean		1.212	7.412	–1.093	-4.904	38.5	21.3	226.8
Atlantic	(60° N→90° N)	0.556	6.926	–1.492	–7.222	1.3	2.7	91.0
	(30° N→60° N)	1.005	7.326	–1.122	–7.857	11.5	10.5	131.6
	(0° N→30° N)	0.232	6.328	–1.153	–4.305	9.1	6.7	272.5
	(30° S→0° N)	0.867	7.233	–0.976	–10.629	9.7	4.2	214.3
	(60° S→30° S)	1.312	7.462	–1.151	–3.330	8.4	8.3	144.1
Pacific	(30° N→60° N)	1.147	7.238	–1.188	2.548	9.5	5.9	165.1
	(0° N→30° N)	0.910	6.895	–1.038	9.756	28.4	9.8	320.0
	(30° S→0° N)	0.816	6.910	–0.882	3.214	29.2	11.8	461.4
	(60° S→30° S)	1.035	7.091	–1.103	5.475	31.9	17.9	187.5
Indian	(0° N→30° N)	1.109	7.456	–0.965	–12.541	3.0	2.0	429.1
	(30° S→0° N)	1.253	7.435	–1.116	-4.532	11.3	8.2	224.4
	(60° S→30° S)	1.311	7.256	–1.179	8.061	10.5	10.3	184.9
Southern	(90° S→60° S)	1.273	7.384	–1.404	-0.510	4.8	5.2	304.0

BGD
6, 7231–7293, 2009

Table 6. As Table 1 except TrOCA optimisation using "C_{ant} -free" regions defined by ventilation age tracer. C_{ant} is assumed zero in these regions and is estimated at peak CFC-11 locations. Optimised values of TrOCA parameters *a*, *b*, *c* and *d* are shown for a range of geographical domains, together with the regional and global C_{ant} inventories that result from their use. The table also includes the corresponding actual C_{ant} simulated by OCCAM. C_{ant} inventories are in Gt C, with negative values of TrOCA estimates set to zero.

Domain		TrOCA parameters				C_{ant} inventory		
		a	*b*	*c*	*d*	Regional		Global
				$\times 10^{-2}$	$\times 10^{5}$	TrOCA	Actual	TrOCA
Default TrOCA		*1.279*	*7.511*	*−1.087*	*7.810*	–	–	*232.4*
World Ocean		1.032	7.282	−1.054	−5.180	188.6	103.5	188.6
Atlantic Ocean		1.232	7.558	−1.095	−11.904	46.7	33.9	173.9
Pacific Ocean		0.970	7.145	−1.033	−0.688	90.4	48.4	212.9
Indian Ocean		1.244	7.533	−1.120	−10.041	31.4	21.3	183.8
Atlantic	(60° N→90° N)	0.853	7.073	−0.746	−2.159	5.6	2.7	88.2
	(30° N→60° N)	1.131	7.418	−1.111	−8.060	12.6	10.5	154.7
	(0° N→30° N)	1.297	7.544	−1.097	−8.723	9.0	6.7	189.5
	(30° S→0° N)	1.281	7.671	−1.126	−16.149	5.7	4.2	180.6
	(60° S→30° S)	1.381	7.578	−1.139	−7.435	10.5	8.3	176.0
Pacific	(30° N→60° N)	1.129	7.331	−1.102	−3.506	8.4	5.9	156.2
	(0° N→30° N)	0.645	6.763	−0.631	−2.347	108.6	9.8	1357.8
	(30° S→0° N)	0.782	7.041	−0.828	−6.816	42.9	11.8	671.8
	(60° S→30° S)	1.269	7.484	−1.132	−6.345	27.7	17.9	173.0
Indian	(0° N→30° N)	0.962	7.312	−0.878	−12.441	5.6	2.0	746.4
	(30° S→0° N)	1.177	7.513	−1.079	−12.007	11.2	8.2	267.9
	(60° S→30° S)	1.397	7.473	−1.185	−0.968	12.7	10.3	214.3
Southern	(90° S→60° S)	1.386	7.519	−1.295	−3.882	3.6	5.2	263.6

Table 7. As Table 6 except C_{ant} is integrated only in regions where ventilation age is below 173 years.

Domain		TrOCA parameters				C_{ant} inventory		
						Regional		Global
		a	*b*	*c* $\times 10^{-2}$	*d* $\times 10^{5}$	TrOCA	Actual	TrOCA
Default TrOCA		*1.279*	*7.511*	*−1.087*	*7.810*	–	–	*232.4*
World Ocean		1.032	7.282	−1.054	−5.180	180.6	103.5	180.6
Atlantic Ocean		1.232	7.558	−1.095	−11.904	45.2	33.9	168.8
Pacific Ocean		0.970	7.145	−1.033	−0.688	87.0	48.3	198.5
Indian Ocean		1.244	7.533	−1.120	−10.041	31.2	21.3	177.3
Atlantic	(60° N→90° N)	0.853	7.073	−0.746	−2.159	5.5	2.7	87.1
	(30° N→60° N)	1.131	7.418	−1.111	−8.060	12.5	10.5	152.4
	(0° N→30° N)	1.297	7.544	−1.097	−8.723	7.7	6.7	176.7
	(30° S→0° N)	1.281	7.671	−1.126	−16.149	5.7	4.2	176.4
	(60° S→30° S)	1.381	7.578	−1.139	−7.435	10.4	8.3	160.5
Pacific	(30° N→60° N)	1.129	7.331	−1.102	−3.506	7.7	5.9	151.9
	(0° N→30° N)	0.645	6.763	−0.631	−2.347	24.8	9.8	932.5
	(30° S→0° N)	0.782	7.041	−0.828	−6.816	26.6	11.8	525.8
	(60° S→30° S)	1.269	7.484	−1.132	−6.345	27.7	17.9	165.3
Indian	(0° N→30° N)	0.962	7.312	−0.878	−12.441	2.2	2.0	544.5
	(30° S→0° N)	1.177	7.513	−1.079	−12.007	10.6	8.2	246.7
	(60° S→30° S)	1.397	7.473	−1.185	−0.968	12.5	10.3	161.3
Southern	(90° S→60° S)	1.386	7.519	−1.295	−3.882	3.6	5.2	219.6

BGD
6, 7231–7293, 2009

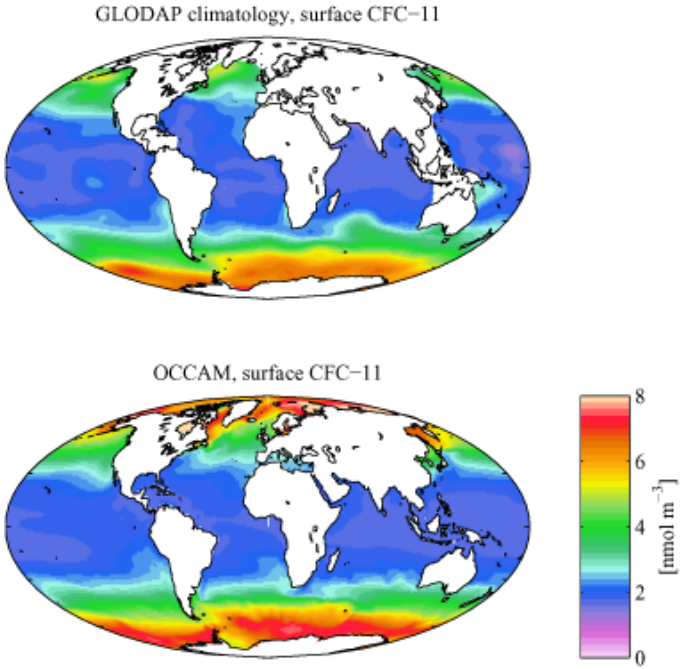

Fig. 1. Comparison of observed (GLODAP; Key et al., 2004) and OCCAM simulated surface CFC-11 concentrations. The GLODAP climatology incorporates observations over a period of years and is nominally "1990s". The OCCAM field shown is the annual average of simulated 1995. Concentrations in nmol m^{-3}. Note that the GLODAP climatology is missing data in regions including the Malay Archipelago, and the Arctic, Caribbean and Mediterranean seas.

BGD
6, 7231–7293, 2009

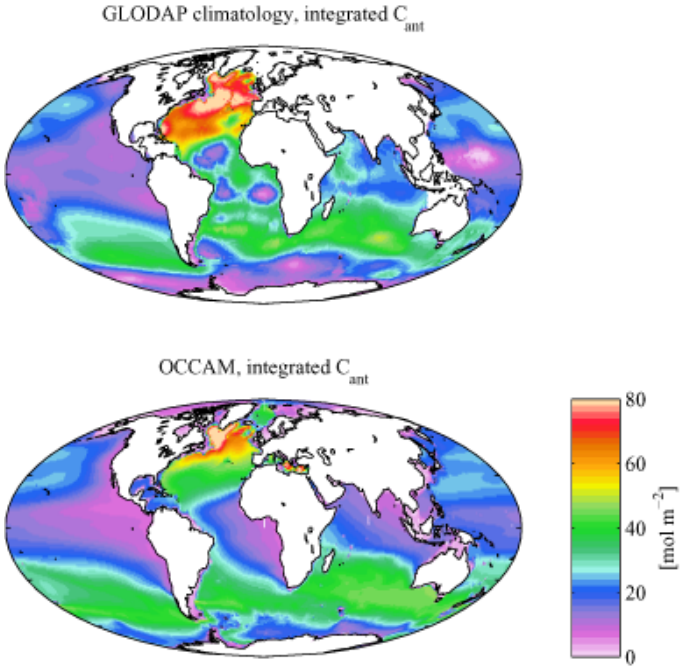

Fig. 2. Comparison of observed (GLODAP; Key et al., 2004) and OCCAM simulated vertically-integrated C_{ant}. The GLODAP climatology incorporates observations over a period of years and is nominally "1990s". The OCCAM field shown is derived from the annual average of simulated 1995. Integrals in mol m^{-2}.

BGD
6, 7231–7293, 2009

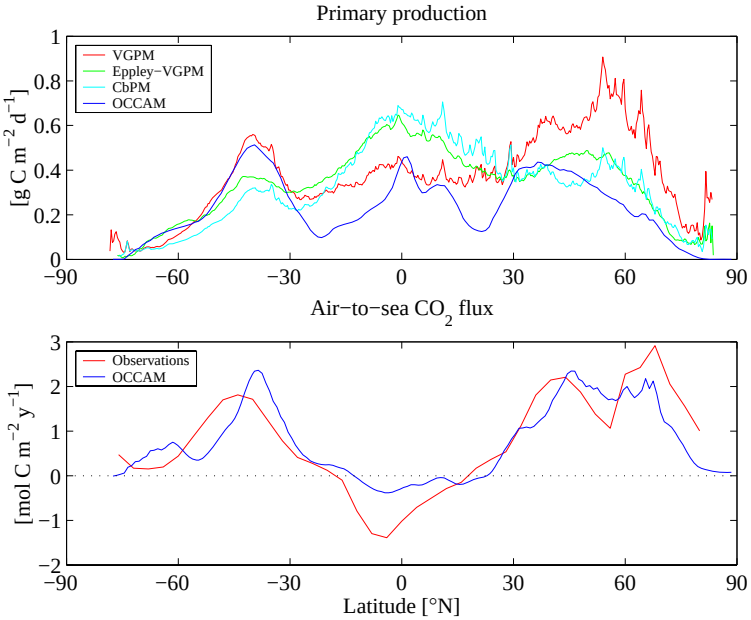

Fig. 3. Comparison of zonally-averaged observational and model fields of primary production (upper) and air-sea CO_2 flux (lower). Primary production observations are derived by applying the VGPM (Behrenfeld and Falkowski, 1997), Eppley-VGPM (Carr et al., 2006) and CbPM (Westberry et al., 2008) productivity models to SeaWIFS fields of surface chlorophyll for the period 2003 to 2004. Air-sea CO_2 flux observations are those estimated by Takahashi et al. (2002) for the standardised year 1995. The corresponding model output are the averages of these fields for the matching periods.

BGD
6, 7231–7293, 2009

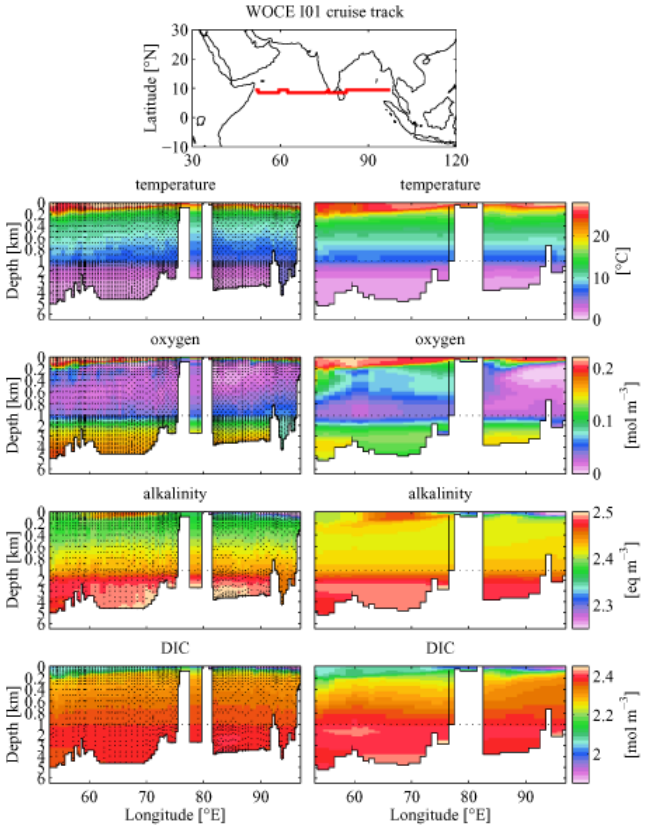

Fig. 4. Observed (left column) and simulated (right column) sections of selected ocean tracers used in the TrOCA method along WOCE cruisetrack I01 (shown in the uppermost panel). Observational fields have been interpolated from the measurement positions indicated (black dots). Note that the vertical scale of the section panels has been altered such that the upper 1000 m is given an expanded scale for clarity.

BGD
6, 7231–7293, 2009

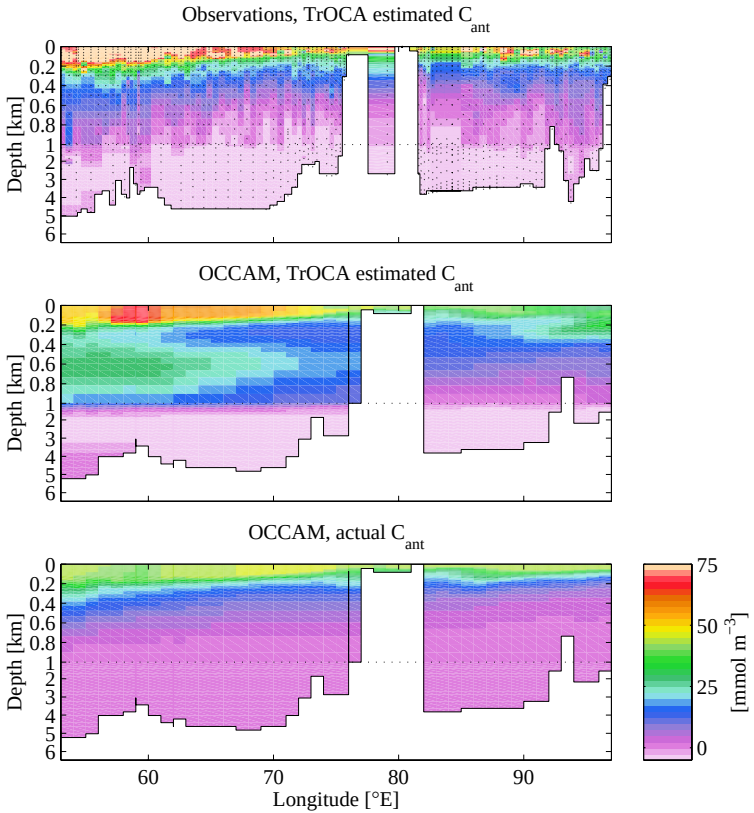

Fig. 5. As Fig. 4 but showing TrOCA estimated C_{ant} from observational fields (top), TrOCA estimated C_{ant} from OCCAM output (middle) and actual OCCAM C_{ant} (bottom). C_{ant} in mmol m^{-3}. Note that the colour scale permits negative C_{ant} concentrations.

BGD
6, 7231–7293, 2009

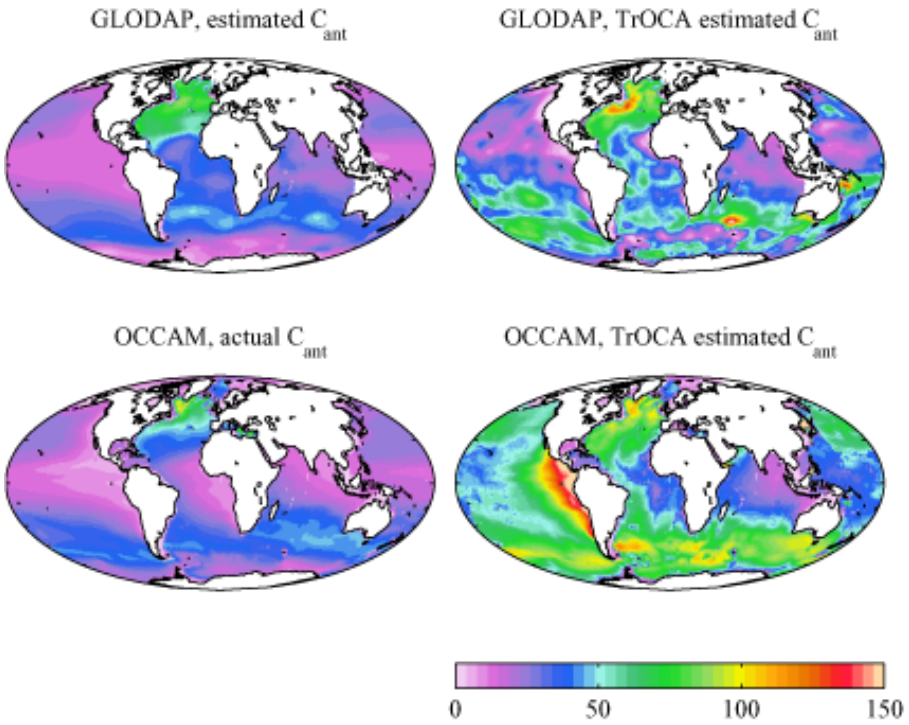

Fig. 6. Comparison of vertically-integrated C_{ant} between observational (GLODAP-estimated; top left) and OCCAM simulated (bottom left) C_{ant} fields and those estimated by default TrOCA (top/bottom right). The observational field is that estimated by GLODAP (Key et al., 2004), and the corresponding TrOCA estimate is based on World Ocean Atlas (Conkright et al., 2002) and GLODAP (Key et al., 2004) climatology fields. Integrals are in mol m^{-2}. Note that negative values of estimated C_{ant} are set to zero before integration.

BGD
6, 7231–7293, 2009

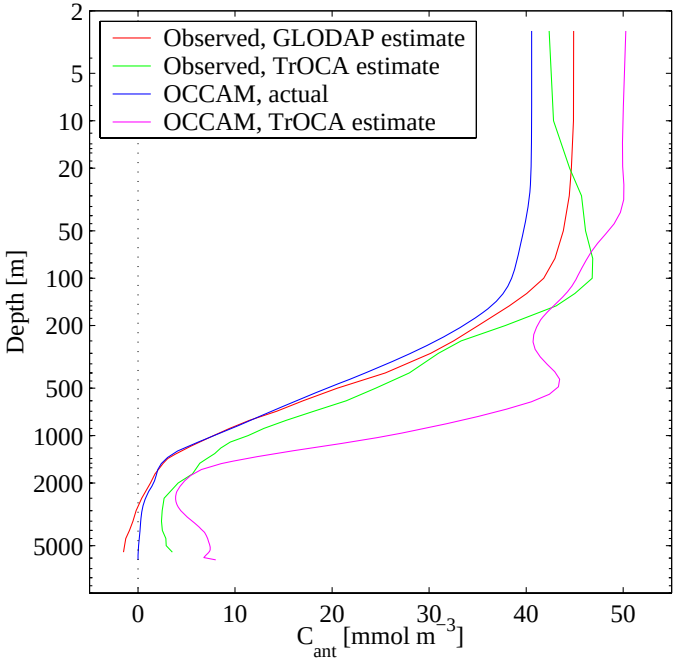

Fig. 7. Globally averaged vertical profiles of observationally-driven GLODAP (red) and default TrOCA (green) estimates of C_{ant}, together with OCCAM simulated C_{ant} (blue) and default TrOCA's corresponding estimate (magenta). Depth is shown on a logarithmic scale to more clearly separate C_{ant} concentrations in near-surface waters. Note that negative values of TrOCA estimated C_{ant} are set to zero before integration.

BGD
6, 7231–7293, 2009

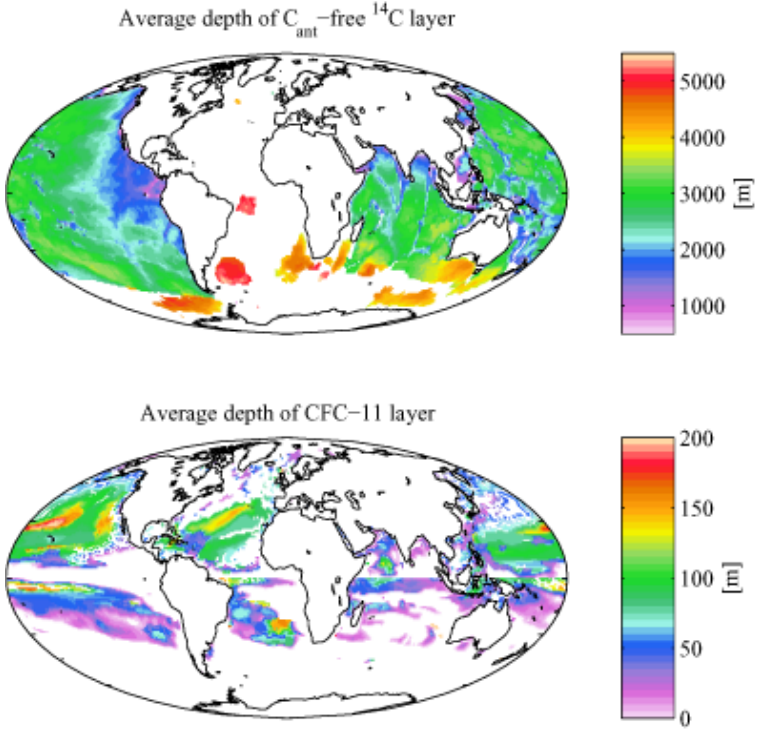

Fig. 8. Average depth of OCCAM grid cells from which tracer output is pooled for TrOCA optimisation. The upper panel shows the data pool (ostensibly C_{ant}-free) derived from ^{14}C distribution. The lower panel shows the data pool (ostensibly C_{ant} contaminated) derived from CFC-11 distribution. The weak discontinuity between the northern and southern hemispheres is due to the use of slightly different CFC-11 criteria in these regions. This is because CFC-11 atmospheric time history is slightly lagged in the southern hemisphere. Depth in m.

BGD
6, 7231–7293, 2009

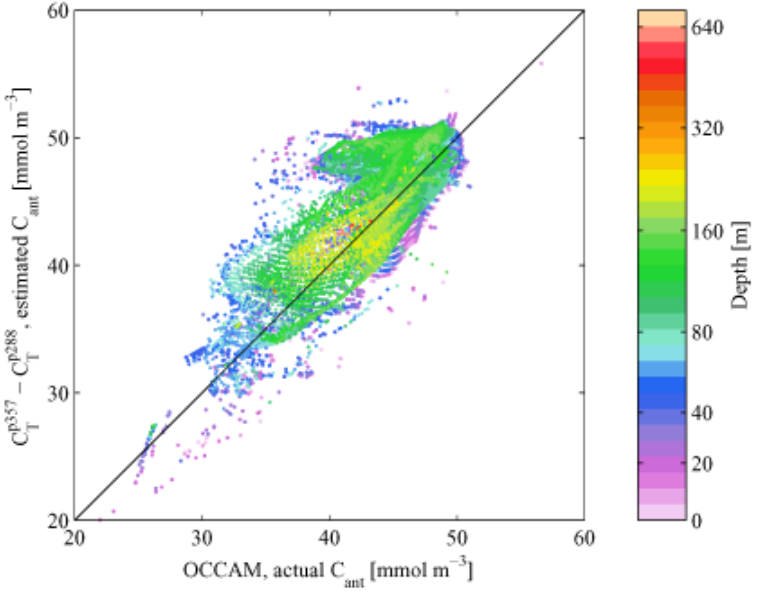

Fig. 9. A comparison of estimated C_{ant} ($C_T^{p357} - C_T^{p288}$) with OCCAM actual C_{ant} for the CFC-11 waters identified in Fig. 8. Colour denotes the depth from which the sample is drawn. The solid line indicates the 1:1 relationship. Concentrations in mmol m^{-3}.

BGD
6, 7231–7293, 2009

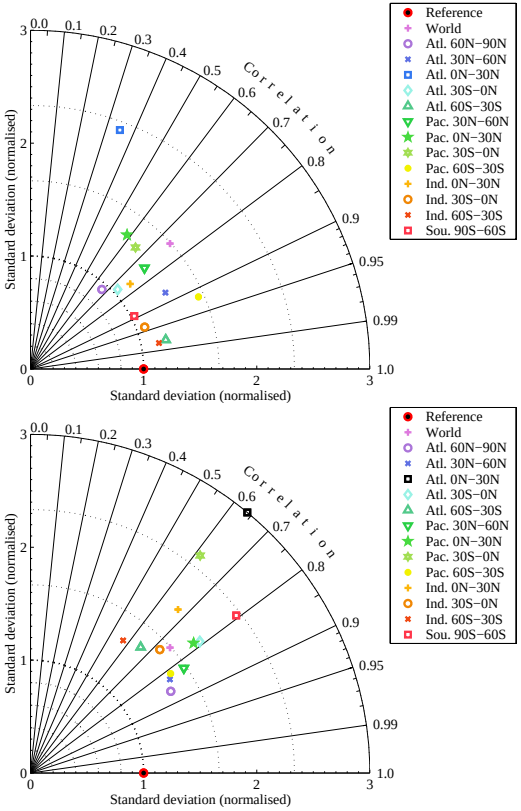

Fig. 10. Taylor diagrams of regional (top) and global (bottom) performance of TrOCA variants optimised using estimated C_{ant}. Symbols refer to variants optimised using regional calibration datasets. Standard deviations are normalised such that actual, OCCAM simulated C_{ant} (labelled here as reference) is exactly 1. This reference value is singular in the case of the global plot (i.e. only one global domain), but multiple in the case of the regional plot (i.e. one per regional domain; because of normalisation, these all overlie one another). Black symbols denote variants with standard deviations outside the plotted range; the symbols are shown at the limit of this range to illustrate correlation.

BGD
6, 7231–7293, 2009

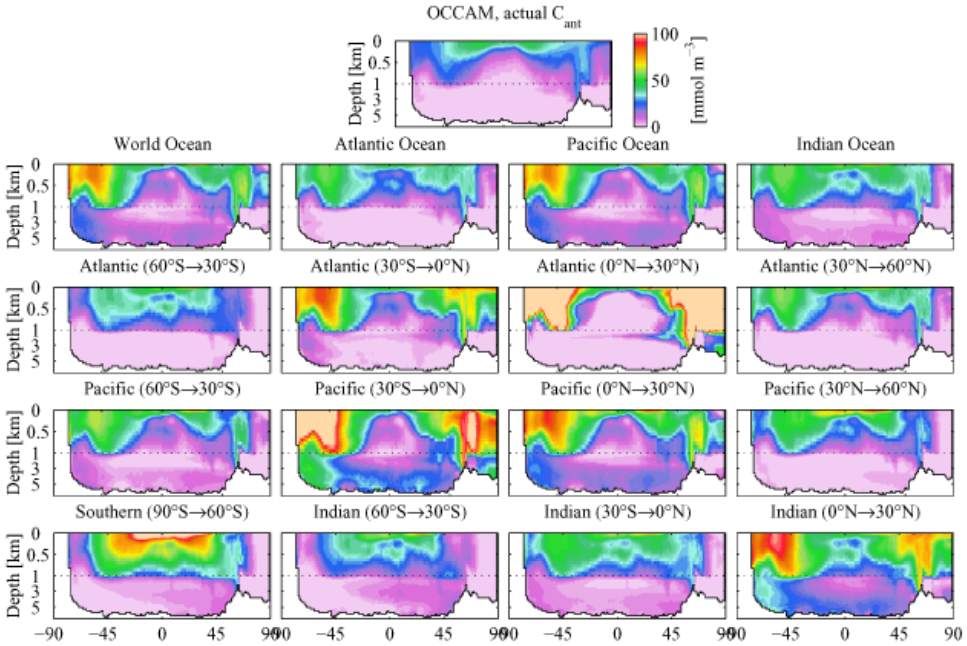

Fig. 11. World Ocean zonally averaged C_{ant} for OCCAM and a selection of TrOCA variant estimates (optimised using estimated C_{ant}). Actual, OCCAM simulated C_{ant} is shown in the top panel, with subsequent rows of panels showing TrOCA variants. C_{ant} in mmol m^{-3}. Note that negative C_{ant} concentrations in the TrOCA estimates were set to zero prior to averaging.

BGD
6, 7231–7293, 2009

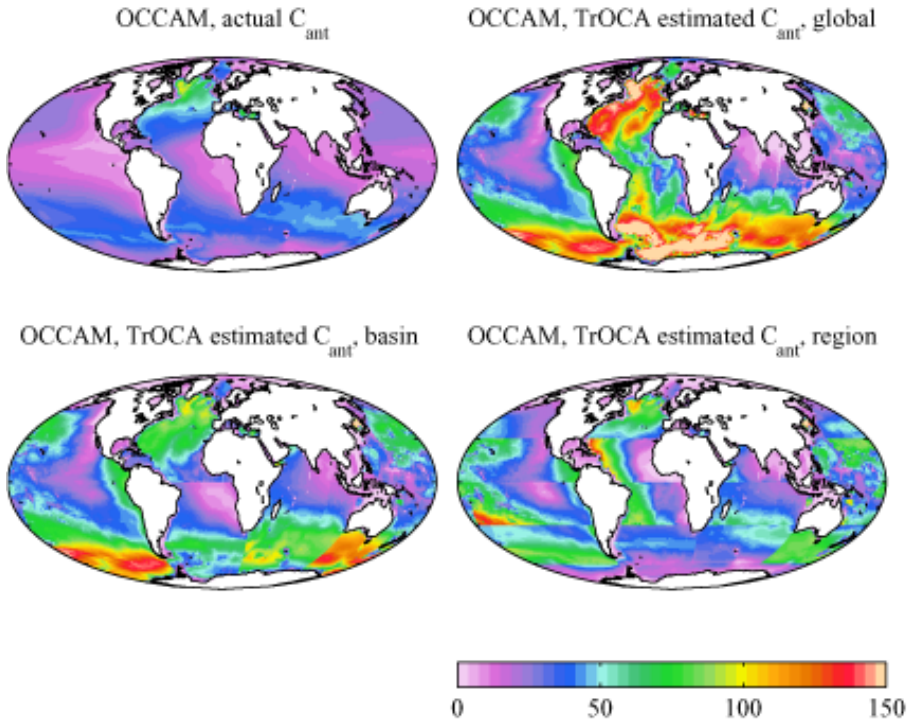

Fig. 12. As Fig. 6 but showing vertically-integrated C_{ant} based on global (top right), basin (bottom left) and regional (bottom right) optimisations. Actual, OCCAM simulated C_{ant} is shown in the top left panel on the same scale. The basin and regional panels show composite maps that combine C_{ant} estimates for particular regions based on the optimised TrOCA variants generated for those regions. C_{ant} in mol m^{-2}. Note that negative values of estimated C_{ant} are set to zero before integration.

BGD
6, 7231–7293, 2009

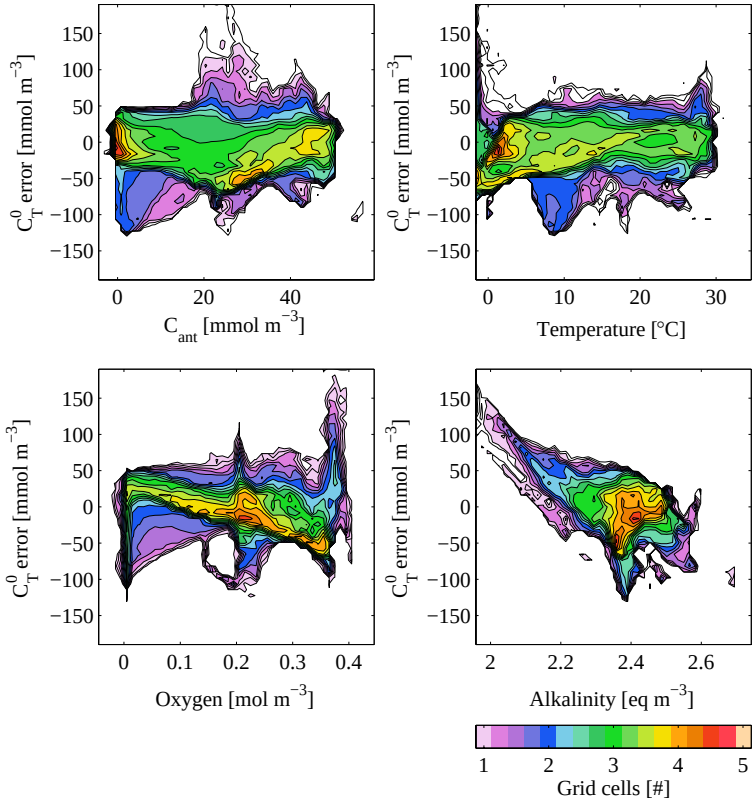

Fig. 13. Error in C_T^0 (estimated – simulated) plotted against actual C_{ant} (top left), potential temperature (top right) oxygen (bottom left) and alkalinity (bottom right). Estimated C_T^0 here is based on the TrOCA variant optimised with the full global calibration dataset. In each case the colour scale is identical and denotes the logarithmic density of OCCAM grid cells (cell volume is ignored here). The plots indicate relationships between TrOCA variant error and the ocean properties used in the TrOCA equation.

BGD
6, 7231–7293, 2009

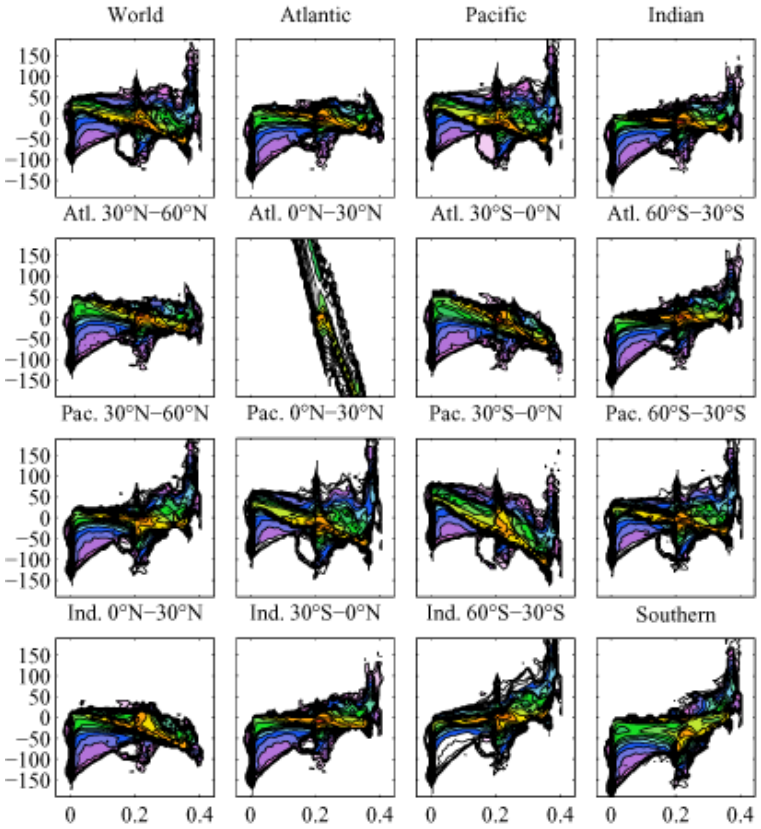

Fig. 14. As Fig. 13 except focusing solely on error in C_T^0 (estimated – simulated) plotted against oxygen concentration. Each panel represents the results from the global application of different TrOCA variants. In each case the colour scale is identical and denotes the logarithmic density of OCCAM grid cells (cell volume is ignored here).

BGD
6, 7231–7293, 2009

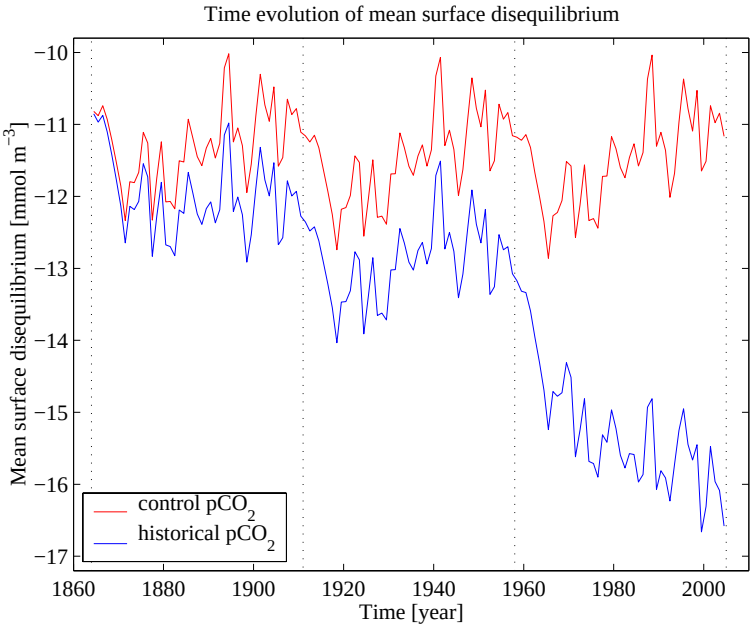

Fig. 15. Globally averaged, surface ocean DIC disequilibrium for control (288 ppm; red) and historical (blue) atmospheric pCO_2 concentrations. Because of the relatively slow equilibriation time of CO_2, the surface ocean is undersaturated in DIC given atmospheric pCO_2. This disequilibrium increases as atmospheric pCO_2 increases due to anthropogenic emissions. The dotted vertical lines denote separate forcing cycles (1958–2004).

BGD
6, 7231–7293, 2009

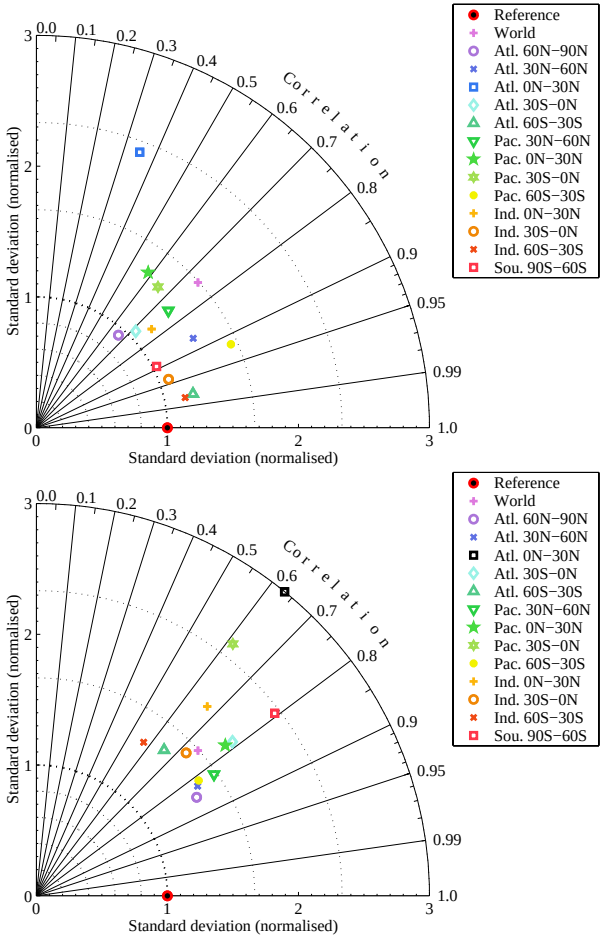

Fig. 16. As Fig. 10 except TrOCA variants optimised using actual OCCAM C_{ant}.

BGD
6, 7231–7293, 2009

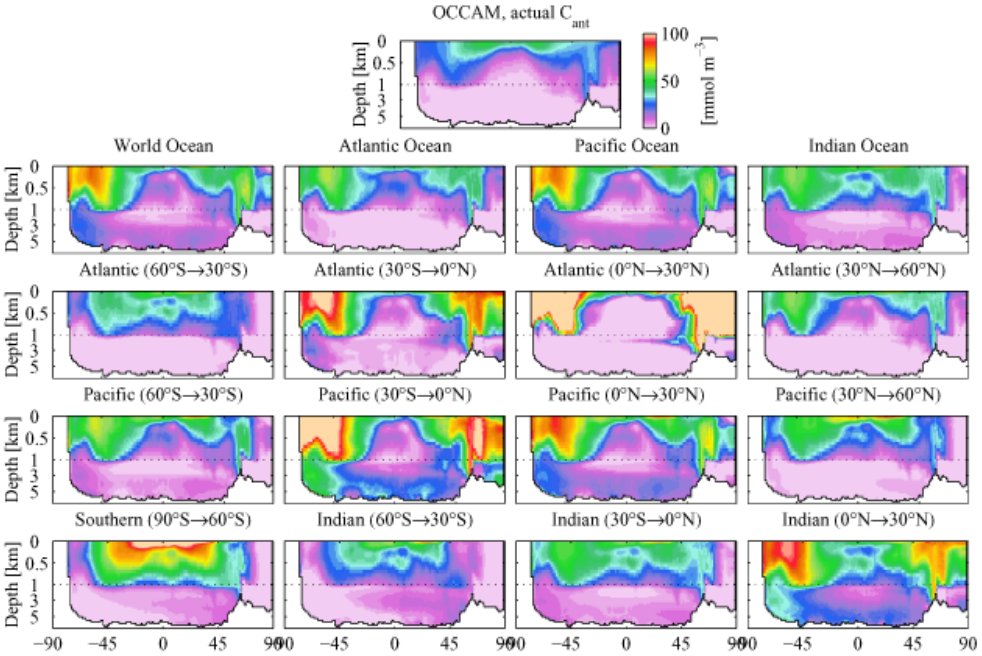

Fig. 17. As Fig. 11 but showing TrOCA variants optimised using actual C_{ant}. C_{ant} in mmol m^{-3}.

BGD
6, 7231–7293, 2009